



Article

Modeling and Experimental Results of Selected Lightweight Complex Concentrated Alloys, before and after Heat Treatment

Dumitru Mitrica ^{1,*} , Ioana Cristina Badea ¹, Mihai Tudor Olaru ^{1,*}, Beatrice Adriana Serban ¹, Denisa Vonica ¹, Marian Burada ¹ , Victor Geanta ², Adrian Nicolae Rotariu ³, Florentin Stoiciu ¹, Viorel Badilita ¹ and Lidia Licu ¹

¹ National R&D Institute for Nonferrous and Rare Metals—IMNR, 102 Biruintei Blvd, Pantelimon, 077145 Ilfov, Romania; cristina.banica@imnr.ro (I.C.B.); beatrice.carlan@imnr.ro (B.A.S.); denisav22@gmail.com (D.V.); mburada@imnr.ro (M.B.); fstoiciu@imnr.ro (F.S.); vbadilita@imnr.ro (V.B.); lidia.licu@imnr.ro (L.L.)

² Faculty of Materials Science and Engineering, University POLITEHNICA of Bucharest, 313 Splaiul Independenței, 6 District, 060042 Bucharest, Romania; victorgeanta@yahoo.com

³ Military Technical Academy, 39-49 George Coșbuc Avenue, 050141 Bucharest, Romania; arotariu99@yahoo.com

* Correspondence: dmitrica@imnr.ro (D.M.); o.mihai@imnr.ro (M.T.O.)

Received: 25 August 2020; Accepted: 25 September 2020; Published: 29 September 2020



Abstract: Lightweight complex concentrated alloys (LWCCA), composed of elements with low density, have become a great area of interest due to the high demand in a large number of applications. Previous research on LWCCAs was focused on high entropy multicomponent alloy systems that provide low density and high capability of solid solution formation. Present research introduces two alloy systems (Al-Cu-Si-Zn-Mg and Al-Mn-Zn-Mg-Si) that contain readily available and inexpensive starting materials and have potential for solid solution formation structures. For the selection of appropriate compositions, authors applied semi-empirical criteria and optimization software. Specialized modeling software (MatCalc) was used to determine probable alloy structures by CALPHAD, non-equilibrium solidification and kinetic simulations. The selected alloys were prepared in an induction furnace. Specimens were heat treated to provide stable structures. Physicochemical, microstructural, and mechanical characterization was performed for the selected alloy compositions. Modeling and experimental results indicated solid solution-based structures in the as-cast and heat-treated samples. Several intermetallic phases were present at higher concentrations than in the conventional alloys. Alloys presented a brittle structure with compression strength of 486–618 MPa and hardness of 268–283 HV. The potential for uniform intermetallic phase distribution in the selected alloys makes them good candidates for applications where low weight and high resistance is required.

Keywords: complex concentrated alloys; low weight; modeling; heat treatment; characterization

1. Introduction

Complex concentrated alloys (CCA) represent a new group of materials, with complex microstructures, comprising of a large number of elements [1]. CCAs extend the established limits of the high entropy alloys (HEAs) concept by allowing a smaller number of elements in the composition and in various proportions, that can deliver mixed structures containing solid solution and well dispersed intermetallic phases. CCAs generally have higher configurational entropy than conventional alloys and are capable of obtaining complex, disordered compositionally complex solid solution structures. CCAs are distinct from conventional alloys in that they are not based on a single major element and

rather include several main elements, which allow a high degree of freedom in alloy compositions and properties. Their properties, such as high temperature resistance, corrosion resistance, workability, and low density, offer a remarkable advantage in the use of CCAs for various extreme conditions applications [2,3].

While no attention was directed to light density CCAs yet, the development of the research in the field of materials science and engineering has focused on the progress of lightweight high-entropy alloys (LWHEA), with superior mechanical and functional properties. Due to their similar design philosophy HEAs are included in the CCA group of alloys, thus a presentation of the most appropriate efforts in developing LWHEA is relevant also to the research of light density complex concentrated alloys.

Several studies in achieving lower density HEA were performed by several authors. Senkov et al. [4,5] studied the microstructure and mechanical properties of low density (up to 6.57 g/cm^3) refractory HEAs. NbTiVZr, NbTiV₂Zr, CrNbTiZr, and CrNbTiVZr alloys were developed by replacing Mo, W, and Ta with Ti, Zr, V, and Cr. Results showed comparable mechanical properties at high temperatures with Inconel 718 and Haynes 230, and CrNbTiVZr largely exceeded the superalloys characteristics (1298 MPa at room temperature and 259 MPa at 1000 °C). Another method for lowering density and improving corrosion resistance in refractory alloys is the addition of Al [6]. Among several compositions, two alloys (AlMo_{0.5}NbTa_{0.5}TiZr and AlNb_{1.5}Ta_{0.5}Ti_{1.5}Zr_{0.5}) have distinguished showing low density (7.4 g/cm^3 and 6.9 g/cm^3 , respectively) and remarkable strength (745 MPa and 403 MPa, respectively) at high temperatures (1000 °C), exceeding IN718 and Mar-M247 performance.

A concentrated effort in the development of low density HEAs involved several research teams. In order to improve the mechanical properties of magnesium alloys Li et al. [7] prepared Mg_x(MnAlZnCu)_{100-x} with variable Mg concentration. The alloys were characterized by high compressive strength (500–400 MPa) and hardness (431–178 HV). The as-cast alloy formed a stable Al-Mn icosahedral quasicrystal phase which is usually met in the alloys obtained by the rapid solidification process.

A high entropy alloy with very low-density (2.67 g/cm^{-3}) was prepared by Youssef et al. [8] by mechanical alloying of elemental powders. The Al₂₀Li₂₀Mg₁₀Sc₂₀Ti₃₀ alloy presented a single-phase structure, with a nanocrystalline grain size of 12 nm and a mechanical hardness of 5.9 GPa.

A different strategy was applied by Feng et al. [9] in selecting LWHEA by the gradual additions of Al and Ti to a core group of transitional elements, in equal proportion (CrFeMn). In order to decrease the probability for the formation of intermetallic phases, authors limited the Ti molar ratio to 0.25 and 1. The criteria calculations for solid solution formation did not satisfy the experimental results, which were well defined by the CALPHAD findings. All the alloys contained intermetallic based phases, but with dominant BCC structure in Al_{1.0}CrFeMnTi_{0.25} and Al_{2.0}CrFeMnTi_{0.25} alloys.

Al and Si additions to CuFeMnNi alloy, as well as the influence of cooling rates on the phase constitution of the alloy, were investigated by Kushnerov and Bashev in [10]. Most of the alloy compositions formed single phase FCC structures in the as-cast state. The increase in the cooling rate through rapid solidification negatively influenced the mechanical properties of the alloy.

Tseng et al. [11] developed a LWHEA containing Be, with a predominant solid solution structure and low level of intermetallic phases, obtained by arc melting. The Al₂₀Be₂₀Fe₁₀Si₁₅Ti₃₅ (atomic percentage composition) alloy delivered unique mechanical properties and oxidation resistance which makes them appropriate for applications in the transportation industry.

Sanchez et al. [12] studied three lightweight high entropy alloys Al₄₀Cu₁₅Cr₁₅Fe₁₅Si₁₅, Al₆₅Cu₅Cr₅Si₁₅Mn₅Ti₅ and Al₆₀Cu₁₀Fe₁₀Cr₅Mn₅Ni₅Mg₅ (atomic percentage composition), which were previously designed by CALPHAD modeling. The alloys were produced by large scale vacuum die casting. Even if the cooling rate of the alloys was very low, the number of phases predicted by Thermo-Calc software was larger than those found in the experimental samples. The obtained alloys presented a high hardness to density ratio, due to the presence of complex precipitates in the as-cast structure.

Most of the literature reports in the field of LWHEA were discussing the formation of single-phase or predominant solid solution structures, in compositions containing elements with low density and with capability to form solid solutions. Other elements with considerable higher density were also included to avoid a high proportion of intermetallic phases. Nevertheless, light density metals are generally very reactive and easily form unwanted oxides and/or intermetallic compounds in the resulted alloy structures. In this respect, there are few metals that can be successfully used for the design of LWHEA. Al, Si, Mg, Ti, Li, Sc, and Be are few of more accessible elements to include in alloys that could be destined to industrial processing. Previous efforts in alloying exclusively light-density elements were limited to the obtaining by nonequilibrium methods such as mechanical alloying [13], which would increase substantially the cost of the final product. Most of the LWHEA prepared by furnace melting were limited to a composition containing Al, Si, Mg, Ti, or Be, with the addition of higher density elements, such as Cu, Fe, Mn, Cr, and Ni, which determined an increase in alloy's density. However, the obtained alloys presented improved properties, exceeding the conventional alloys characteristics and presented a promising approach in the continuously demanding field of materials design.

In order to determine the most relevant HEA compositions, a set of theoretical and empirical criteria was developed by several authors [14–21]. The formation of predominant solid solution phases and moreover the obtaining of single phase HEAs, based on specific elemental combinations, were studied by a semiempirical approach, where the theoretical criteria were combined with experimental findings. Hume-Rothery rule applied to the high entropy alloys showed that for atomic size difference (δ) less than 6.6 [15,16] and Allen electronegativity difference ($\Delta\chi_{\text{Allen}}$) between 3 and 6 [17,18], solid solution structures will be preferentially formed in as-cast alloys. The valence electron concentration (VEC) determined the type of solid solution structure which is FCC for VEC less than 6.87, a mix of FCC and BCC structures found if $6.87 < \text{VEC} < 8$, and predominant BCC structures should appear if VEC is higher than 8 [19]. Thermodynamic parameters like enthalpy of mixing ($-11.6 \text{ kJ/mol} < \Delta H_{\text{mix}} < 3.2 \text{ kJ/mol}$), entropy of mixing ($11 \text{ J/mol}\cdot\text{K} < \Delta S_{\text{mix}} < 19.5 \text{ J/mol}\cdot\text{K}$) or ratio between them ($1.1 < \Omega$), are other types of criteria, which are also used to determine solid solution formation in high entropy alloys [15,20]. A separate criterion based on the influence of the atomic size difference on the mixing entropy of the system has been determined and named geometric parameter Λ , which shows that predominant solid solutions are formed for $\Lambda < 0.24$, while single phase solid solution forms when $\Lambda > 0.96$ [21]. The mentioned criteria are not exhaustive and are not meant to be effective on any CCA system, as was proven before in referenced papers.

CALPHAD is another method for selecting HEA compositions, that implies complex computer modeling, based on thermodynamic calculations and empirical data. The method was proposed, performed, and recommended by several authors [22–26]. CALPHAD method paired with established semi-empirical criteria and diffusion modeling is able to offer a sustainable approach in selecting most viable compositions. The calculation results can be than compared to the experimental findings.

The present study investigates several lightweight complex concentrated alloys (LWCCA) composed of readily available elements, that are widely used in conventional alloys, based on Al-Cu-Si-Zn-Mg and Al-Mn-Zn-Mg-Si systems. Our purpose was to design a proper alloy with inexpensive lightweight elements, who can be obtained with ease by traditional manufacturing processes. Alloy design tools were used to predict structural behavior before and after the heat treatment process and experimental trials were performed for the selected alloys.

2. Materials and Methods

In order to reach the desired physical and mechanical properties, it is very important to find a suitable composition of the alloy. The properties of CCAs are specifically influenced by the constitutive elements. A vast majority of lightweight high-entropy alloys contain elements like Al, Si, Mg, Ti, and B in order to reduce alloy density. In order to avoid alloy brittleness due to poor machinability, elements like Cu, Zn, and Mn were selected as most appropriate. Although, these elements are

not known as having low density, they are able to form stable solid solutions with lighter elements. Thus, Mn favour formation of complex solid solutions and Cu induces high machinability of the material by increasing deformability.

Selection of most appropriate compositions was performed by the optimization of semi-empirical criteria. The semi-empirical criteria are defined by the following relations:

- a. The entropy of mixing (ΔS_{mix}) is calculated using Boltzmann's equation

$$\Delta S_{\text{mix}} = -R \times \sum c_i \times \ln c_i \quad (1)$$

where R is the gas constant (8.314 J/mol·K) and c_i is the molar fraction for element i ,

- b. The enthalpy of mixing (ΔH_{mix}) is calculated with a formula derived from the Miedema macroscopic model [27]

$$\Delta H_{\text{mix}} = \sum 4c_i c_j \times \Delta H_{ij} \quad (2)$$

where ΔH_{ij} is the binary enthalpy of mixing for elements i and j

- c. The atomic size difference (δ) was defined by [14]

$$\delta = 100 \times \sqrt{\sum c_i \times \left(1 - \frac{r_i}{\bar{r}}\right)^2} \quad (3)$$

where r_i is the atomic radius of element i , \bar{r} is the average atomic radius.

- d. The derived parameter Ω , which includes the influence of both ΔS_{mix} and ΔH_{mix} [15], was calculated with

$$\Omega = T_m \Delta S_{\text{mix}} / |\Delta H_{\text{mix}}| \quad (4)$$

where T_m is the melting temperature calculated with $T_m = \sum c_i \times T_{mi}$, and T_{mi} is the melting temperature of element i .

- e. The formula for electronegativity difference after Allen ($\Delta\chi$) was deduced as follows [17]

$$\Delta\chi = 100 \times \sqrt{\sum c_i \times \left(1 - \frac{\chi_i}{\bar{\chi}}\right)^2} \quad (5)$$

where χ_i is the Pauling electronegativity of element i and $\bar{\chi}$ is the average electronegativity.

- f. The valence electron concentration (VEC) is used for determining the type of solid solution formed in the alloy. VEC is calculated with an equation based on element concentration and individual VEC [19]

$$VEC = \sum c_i \times VEC_i \quad (6)$$

where VEC_i is the valence electron concentration of element i .

- g. The geometrical parameter (Λ) that defines the ration between mixing entropy and atomic size difference of the alloy [21]

$$\Lambda = \Delta S_{\text{mix}} / \delta^2 \quad (7)$$

The properties for the elements that enter the calculations were acquired from valuable sources, suggested by the authors that originally developed the criteria, such as: atomic radius [28], Allen electronegativity [29,30], melting temperatures [31], and pair mixing enthalpy [32].

The optimization of the alloy compositions was performed by means of the multi-objective optimization module from MATLAB software (version 6.02, MatCalc Engineering GmbH, Vienna, Austria).

MatCalc Pro edition, version 6.02, was used for multi-component phase equilibrium and thermodynamics by CALPHAD method, as well as non-equilibrium solidification and multi-phase precipitation kinetics.

The optimal alloy compositions were prepared in an induction furnace type Linn MFG-30 (Linn High Therm GmbH, Eschenfelden, Germany) with inert atmosphere and cast in a copper mould. Technical purity raw materials of Al, Cu, Si, Zn, Mg, and Mn were used in the experimental trials. A 350 g charge for each alloy was placed in an alumina-based crucible. The alloys were melted in the induction furnace and cast in a copper mould, under protective atmosphere. The resulted as-cast alloys were annealed in an electrical furnace, LHT 04/17 Nabertherm GMBH (Lilienthal, Germany), under protective atmosphere (Ar). The heat treatment stage was conducted at 400 °C for 20 h, with slow cooling rate of 3 °C/min. Samples were taken before and after the heat treatment process for chemical, structural, and mechanical analyses.

The chemical composition of the alloys was determined by inductively coupled plasma spectrometry (ICP-OES) using an Agilent 725 spectrometer (Santa Clara, CA, USA). Samples from various places of the alloy ingot were investigated. Optical microscopy investigation was performed with a Zeiss Axio Scope A1m Imager microscope (Jena, Germany) with bright field, dark field, DIC and polarization capabilities, and high contrast EC Epiplan 109/509/1009 lenses. Image analyzer software ImageJ vers. 1.53e, developed by W. Rasband, U. S. National Institutes of Health, Bethesda, MD, USA, was used to count porosity and shrinkage in the specimens. Samples were previously etched with a Keller type solution (prepared on-site) to enhance the visibility of the grains and the grain boundaries. Scanning electron microscopy (SEM) was performed with a FEI Quanta 3D FEG microscope (FEI Europe B.V., Eindhoven, Netherlands), operating at 20–30 kV, equipped with an energy dispersive X-ray spectrometer (EDS). The phase configuration was analyzed by X-ray diffractometry (XRD) (FEI Europe B.V., Eindhoven, Netherlands). Data acquisition was performed on BRUKER D8 ADVANCE diffractometer (Bruker Corporation, Billerica-MA, USA), using DIFFRAC^{plus} XRD Commander (Bruker AXS) software (version 2018, Bruker Corporation, Billerica-MA, USA), Bragg-Brentano diffraction method, Θ - Θ coupled in vertical configuration, with the following parameters: CuK α radiation, 2Θ Region: 20–1240, 2Θ Step: 0.020, Time/step: 8.7 s/step, rotation speed 15 rot/min, CuK β radiation was removed with SOL X detector (Bruker Corporation, Billerica, MA, USA). The resulting data was processed using Bruker[®] Diffracplus EVA Release 2018 software to search the database ICDD[®] Powder Diffraction File (PDF4+, 2019 edition) and the full pattern matching (FPM) module of the same software package. The semi-quantitative evaluation was performed by the RIR method (reference intensity ratio) of the identified phase concentrations.

Compression strength for both alloys was determined with a LBG testing machine, model TC-100 (LBG testing equipment srl, Azzanos, Paolo, Italy), with max load of 100 kN. The testing samples were alloy bars with 6 mm in diameter and 6 mm length. The compression speed was 6 mm/min.

Vickers microhardness of the samples was measured at room temperature using microindenter attachment (Anton Paar MHT10, Anton Paar GmbH, GRAZ, Austria), with an applied load of 2 N and slope of 0.6 N/s. Ten measurements were made for each sample to determine the average values.

3. Results

3.1. Criteria Calculation

The criteria calculations were performed for the Al-Cu-Si-Zn-Mg and Al-Mn-Zn-Mg-Si systems (Table 1) with the variation of each element composition in a relevant interval, appropriate to the high entropy concept. Each element from the alloy composition was varied separately from 0.5 to 2.5 molar concentrations, according to the high entropy alloy conventions (1 is the value for equal composition).

Table 1. Criteria calculation results for AlCuSiZnMg and AlMnZnMgSi systems.

Nr	Alloy	Composition						$\Delta\chi_{\text{Allen}}\%$	Ω	Λ (J/mol·K)	ρ (g/cm ³)
		Al	Cu	Si	Zn	Mg	Mn				
1	Al _{0.5} CuSiZnMg	11.2	22.2	22.2	22.2	22.2	-	14.08	1.00	0.10	3.48
2	AlCuSiZnMg	20	20	20	20	20	-	13.42	1.09	0.11	3.39
3	Al _{1.5} CuSiZnMg	27.3	18.2	18.2	18.2	18.2	-	12.85	1.15	0.12	3.32
4	Al ₂ CuSiZnMg	33.3	16.7	16.7	16.7	16.7	-	12.34	1.19	0.13	3.26
5	Al _{2.5} CuSiZnMg	38.5	15.4	15.4	15.4	15.4	-	11.89	1.23	0.13	3.21
6	AlCuSi _{0.5} ZnMg	22.2	22.2	11.1	22.2	22.2	-	13.21	1.52	0.13	3.56
7	AlCuSi _{1.5} ZnMg	18.2	18.2	27.3	18.2	18.2	-	13.41	0.93	0.10	3.26
8	AlCuSi ₂ ZnMg	16.7	16.7	33.3	16.7	16.7	-	13.28	0.85	0.09	3.16
9	AlCuSi _{2.5} ZnMg	15.4	15.4	38.5	15.4	15.4	-	13.09	0.81	0.09	3.08
10	AlCuSiZn _{0.5} Mg	22.2	22.2	22.2	11.1	22.2	-	14.03	1.00	0.10	3.35
11	AlCuSiZn _{1.5} Mg	18.2	18.2	18.2	27.3	18.2	-	12.88	1.16	0.12	3.43
12	AlCuSiZn ₂ Mg	16.7	16.7	16.7	33.3	16.7	-	12.41	1.21	0.13	3.46
13	AlCuSiZn _{2.5} Mg	15.4	15.4	15.4	38.5	15.4	-	11.98	1.25	0.14	3.50
14	AlCuSiZnMg _{0.5}	22.2	22.2	22.2	22.2	11.1	-	11.60	1.10	0.13	3.70
15	AlCuSiZnMg _{1.5}	18.2	18.2	18.2	18.2	27.3	-	14.55	1.07	0.10	3.16
16	AlCuSiZnMg ₂	16.7	16.7	16.7	16.7	33.3	-	15.27	1.06	0.10	2.99
17	AlCuSiZnMg _{2.5}	15.4	15.4	15.4	15.4	38.5	-	15.74	1.04	0.10	2.86
18	AlCu _{0.5} SiZnMg	22.2	11.1	22.2	22.2	22.2	-	13.68	0.97	0.10	2.90
19	AlCu _{1.5} SiZnMg	18.2	27.3	18.2	18.2	18.2	-	13.11	1.18	0.12	3.80
20	AlCu ₂ SiZnMg	16.7	33.3	16.7	16.7	16.7	-	12.79	1.26	0.12	4.16
21	AlCu _{2.5} SiZnMg	15.4	38.5	15.4	15.4	15.4	-	12.47	1.32	0.12	4.47
22	Al _{0.5} MnZnMgSi	11.1	-	22.2	22.2	22.2	22.2	13.34	0.60	0.11	3.92
23	AlMnZnMgSi	20	-	20	20	20	20	12.68	0.64	0.12	3.80
24	Al _{1.5} MnZnMgSi	27.3	-	18.2	18.2	18.2	18.2	12.11	0.66	0.13	3.71
25	Al ₂ MnZnMgSi	33.3	-	16.7	16.7	16.7	16.7	11.61	0.68	0.14	3.63
26	Al _{2.5} MnZnMgSi	38.5	-	15.4	15.4	15.4	15.4	11.17	0.70	0.15	3.56
27	AlMn _{0.5} ZnMgSi	22.2	-	22.2	22.2	22.2	11.1	13.22	0.73	0.11	3.53
28	AlMn _{1.5} ZnMgSi	18.2	-	18.2	18.2	18.2	27.3	12.19	0.58	0.13	4.04
29	AlMn ₂ ZnMgSi	16.7	-	16.7	16.7	16.7	33.3	11.74	0.55	0.14	4.25
30	AlMn _{2.5} ZnMgSi	15.4	-	15.4	15.4	15.4	38.5	11.34	0.53	0.15	4.44
31	AlMnZn _{0.5} MgSi	22.2	-	11.1	22.2	22.2	22.2	13.30	0.57	0.11	3.48
32	AlMnZn _{1.5} MgSi	18.2	-	27.3	18.2	18.2	18.2	12.14	0.69	0.14	4.07
33	AlMnZn ₂ MgSi	16.7	-	33.3	16.7	16.7	16.7	11.66	0.73	0.14	4.30
34	AlMnZn _{2.5} MgSi	15.4	-	38.5	15.4	15.4	15.4	11.23	0.77	0.15	4.49
35	AlMnZnMg _{0.5} Si	22.2	-	22.2	11.1	22.2	22.2	10.91	0.55	0.14	4.12
36	AlMnZnMg _{1.5} Si	18.2	-	18.2	27.3	18.2	18.2	13.76	0.70	0.12	3.56
37	AlMnZnMg ₂ Si	16.7	-	16.7	33.3	16.7	16.7	14.46	0.76	0.11	3.37
38	AlMnZnMg _{2.5} Si	15.4	-	15.4	38.5	15.4	15.4	14.91	0.81	0.11	3.21
39	AlMnZnMgSi _{0.5}	22.2	-	22.2	22.2	11.1	22.2	12.11	0.78	0.16	3.99
40	AlMnZnMgSi _{1.5}	18.2	-	18.2	18.2	27.3	18.2	12.88	0.56	0.11	3.65
41	AlMnZnMgSi ₂	16.7	-	16.7	16.7	33.3	16.7	12.90	0.52	0.10	3.53
42	AlMnZnMgSi _{2.5}	15.4	-	15.4	15.4	38.5	15.4	12.81	0.49	0.09	3.43

The influence of element composition on the main parameters is illustrated in Figures 1 and 2. The optimal ranges for solid solution formation, as presented in the introduction section, are: $\Omega > 1.1$, $\Delta\chi_{\text{Allen}} < 6\%$ and $\Lambda > 24$ J/mol·K. The atomic size mismatch was not represented as is included in the Λ parameter. The range limit is shown on diagrams with a dotted line. The results show that, for a Al-Cu-Si-Zn-Mg system, Mg and Si are decreasing the probability for solid solution formation, while Al, Cu, and Zn have a positive effect. However, Cu and Zn are rather heavy elements and increase the alloy density considerably, which has to be taken into account in final alloy selection. The Al-Mn-Zn-Mg-Si system capability to form solid solutions is strongly improved by the increase of Al concentration. Mn and Zn have also a positive influence on the alloy structure, but less important than Al. Another contradiction is shown here between Ω and Λ parameter, for the Mn and Mg influence. As expected, Si is not a good solid solution former, similar to the effect on Al-Cu-Si-Zn-Mg system.

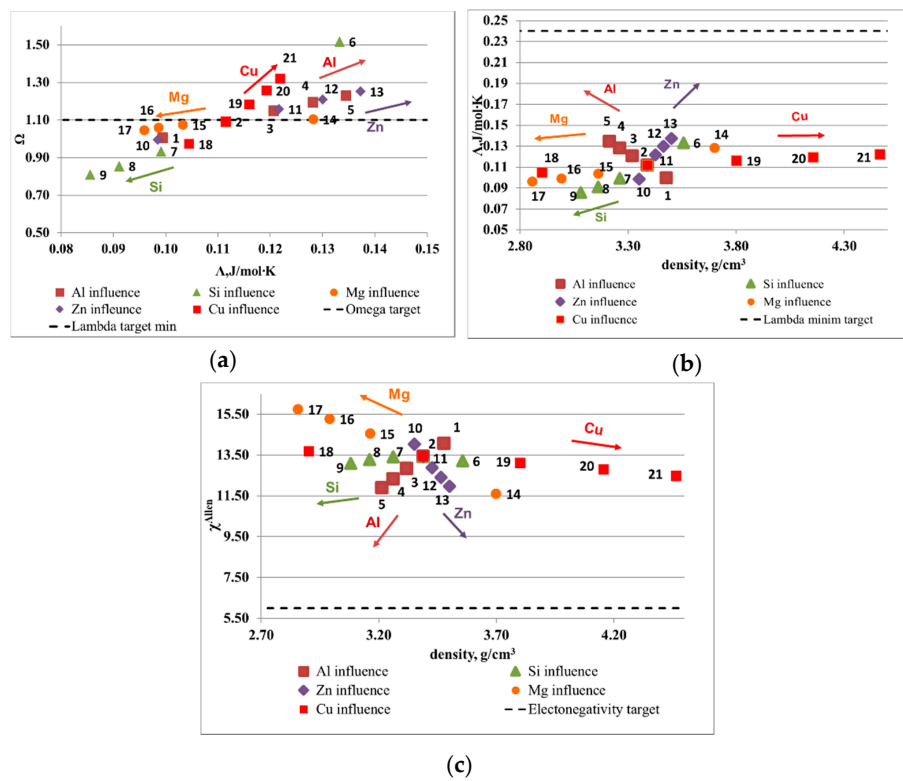


Figure 1. Elemental influence over the criteria values for Al-Cu-Si-Zn-Mg system: (a) Δ versus Ω , (b) Δ versus density, and (c) $\Delta\chi_{Allen}$ versus density.

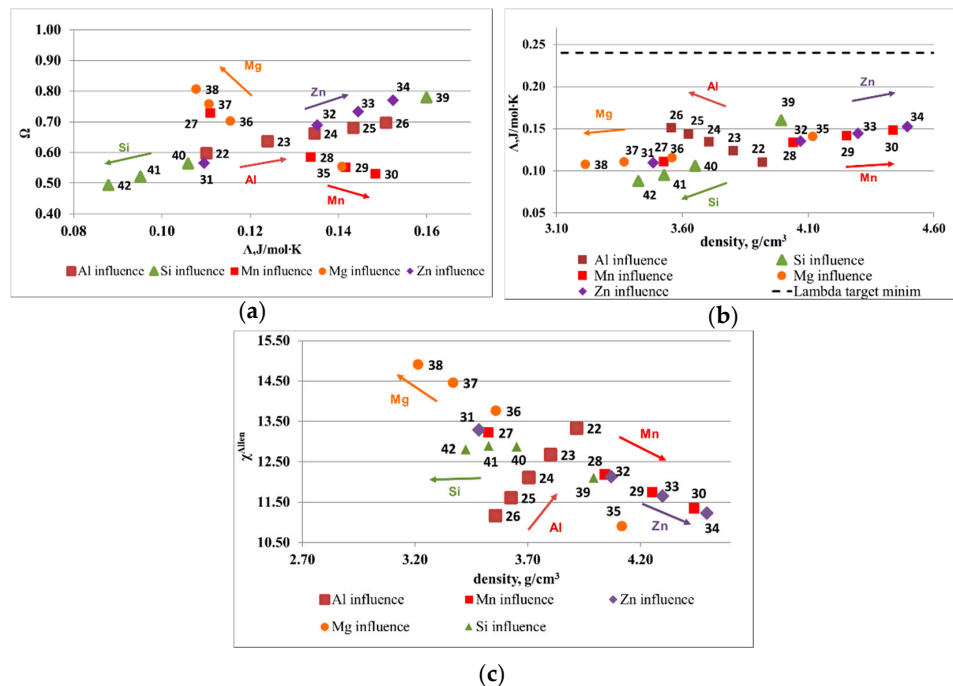


Figure 2. Elemental influence over the criteria values for Al-Mn-Zn-Mg-Si system: (a) Δ versus Ω , (b) Δ versus density, and (c) $\Delta\chi_{Allen}$ versus density.

However, the results showing the influence of each element to the formation of solid solution structures are qualitative in nature and do not show specific alloy compositions that can be further studied for practical use. The influence of the composition elements on the structural behavior is important in material design for determining compositional areas of interest that can be attractive

for different applications. Those areas can then be studied further for the development of optimal compositions with targeted properties.

Taking data acquired in the present research work into consideration, a general approach for the selection of optimal compositions with high probability in the formation of solid solution structures can be performed by the means of special algorithms of global multi-objective optimization process.

In order to select most appropriate compositions for both systems, the equations defined by the established criteria entered a multi-objective optimization process. There are several methods that can be applied to present case scenario for multi-objective optimization. The Pareto front method was selected for increased accuracy. The optimization problem was set for finding the minimum value for the electronegativity difference (Equation (5)) and alloy density (Equation (8)), and the maximum value for the derived parameter Ω (Equation (4)) and geometrical parameter Λ (Equation (7)). The density of the alloy was calculated with formula

$$\frac{1}{\rho} = \sum_{i=1}^n \frac{w_i}{\rho_i \times 100} \quad (8)$$

where ρ is the alloy density, ρ_i is the component metal density, and w_i is the concentration in weight percent (wt.%) of the component metal i .

The problem setup contained the constraints for optimal values, which correspond to the limits for each parameter presented earlier in the introduction section: $\Lambda > 0.24$, $\Omega > 1.1$ and $\Delta\chi_{\text{Allen}} < 6$. The genetic algorithm solver was used with following options: double vector population, feasible population for creation function, adaptive feasibility for the mutation function, and single point crossover function.

Several optimized compositions were determined (Tables 2 and 3) and were illustrated in Figures 3 and 4. For the Al-Cu-Si-Zn-Mg system, several alloy compositions are complying with the solid solution formation criteria. Even if the electronegativity criterion is respected only by two compositions, the rest of the alloys are not far away from the solid solution formation limit. The lowest density was shown by the $\text{Al}_{3.4}\text{Cu}_{0.5}\text{Si}_{0.2}\text{Zn}_{0.5}\text{Mg}_{0.2}$ alloy. The optimal compositions for the Al-Mn-Zn-Mg-Si system present limited availability for solid solution formation structures. Only three out of seven compositions are placed well in the required intervals. Due to the targeted application that originated the research study, an alloy with density close to 3 g/cm^3 was desired. The $\text{Al}_3\text{Mn}_{0.2}\text{Zn}_{0.3}\text{Mg}_{0.7}\text{Si}_{0.8}$ has the lowest density and presents similar criteria values with the other low-density alloys.

Table 2. Multiobjective optimization results for Al-Cu-Si-Zn-Mg system.

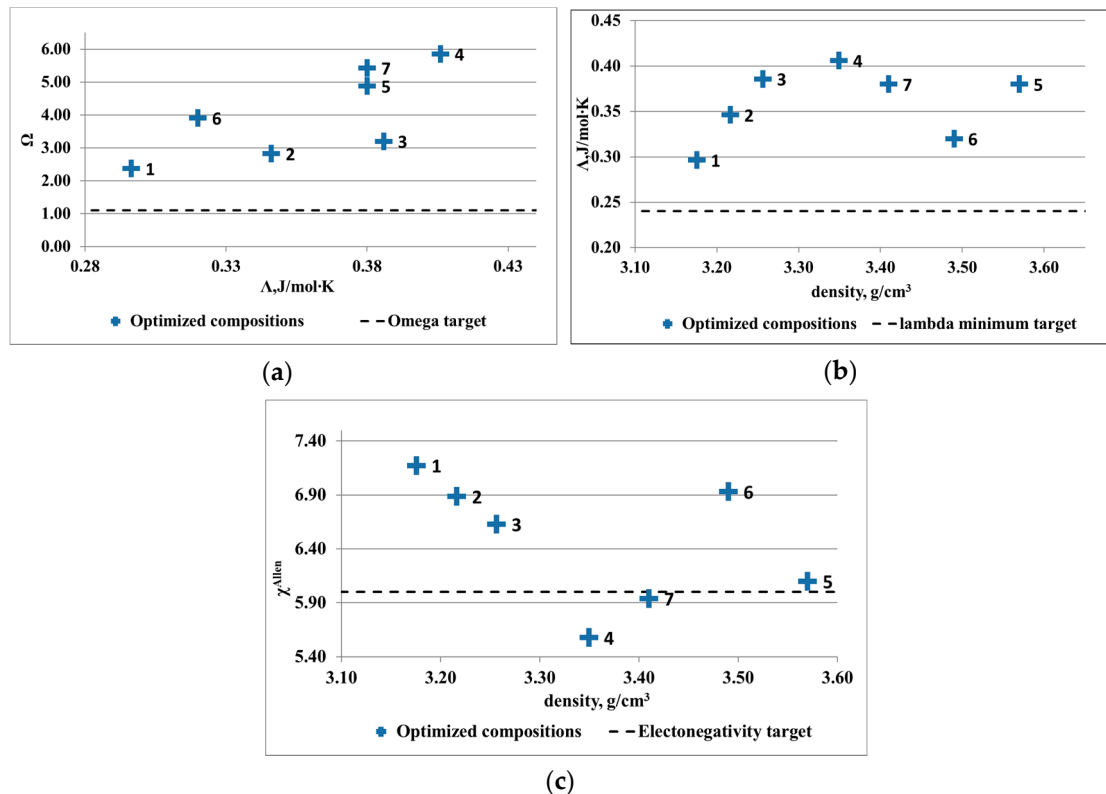
Nr	Optimized Compositions						δ %	$\Delta\chi_{\text{Allen}}$ %	Ω	Λ (J/mol-K)	ρ (g/cm ³)
	Alloy	Al	Cu	at % Si	Zn	Mg					
1	$\text{Al}_{3.4}\text{Cu}_{0.5}\text{Si}_{0.2}\text{Zn}_{0.5}\text{Mg}_{0.2}$	70.8	10.4	4.2	10.4	4.2	5.71	7.17	2.37	0.30	3.18
2	$\text{Al}_{3.4}\text{Cu}_{0.5}\text{Si}_{0.2}\text{ZnMg}_{0.2}$	64.2	9.4	3.8	18.9	3.8	5.45	6.89	2.82	0.35	3.22
3	$\text{Al}_{3.4}\text{Cu}_{0.5}\text{Si}_{0.2}\text{Zn}_{1.5}\text{Mg}_{0.2}$	58.6	8.6	3.4	25.9	3.4	5.22	6.63	3.20	0.39	3.26
4	$\text{Al}_4\text{Cu}_{0.15}\text{Si}_{0.1}\text{Zn}_{0.7}\text{Mg}_{0.3}$	77.7	2.9	1.9	13.6	3.9	4.04	5.58	5.86	0.41	3.35
5	$\text{Al}_3\text{Cu}_{0.2}\text{Si}_{0.1}\text{Zn}_{0.7}\text{Mg}_{0.2}$	71.4	4.8	2.4	16.7	4.8	4.51	6.10	4.88	0.38	3.57
6	$\text{Al}_3\text{Cu}_{0.3}\text{Si}_{0.1}\text{Zn}_{0.6}\text{Mg}_{0.3}$	69.8	7	2.3	14	7	5.05	6.93	3.91	0.32	3.49
7	$\text{Al}_3\text{Cu}_{0.2}\text{Si}_{0.1}\text{Zn}_{0.8}\text{Mg}_{0.2}$	69.8	4.7	2.3	18.6	4.7	4.29	5.94	5.43	0.38	3.41

3.2. CALPHAD Modeling

The CALPHAD method is using thermodynamic and kinetic data and equations to determine Gibbs free energies and diffusion mobility characteristics of a system [22]. Phase stability parameters and phase composition can be determined function of alloy composition and system temperature. Recent improvements of alloys databases allow for the obtaining of pertinent results when using CALPHAD based software.

Table 3. Multiobjective optimization results for Al-Mn-Zn-Mg-Si system.

Nr	Optimized Compositions						δ %	$\Delta\chi_{\text{Allen}}$ %	Ω	Λ (J/mol-K)	ρ (g/cm ³)
	Alloy	Al	Mn	at % Si	Zn	Mg					
1	Al ₃ Mn _{0.2} Zn _{0.5} Mg _{0.5} Si _{0.5}	63.8	4.3	10.6	10.6	10.6	7.55	9.14	0.37	0.17	3.08
2	Al ₃ Mn _{0.3} Zn _{0.2} Mg _{0.6} Si _{0.6}	63.8	6.4	12.8	4.3	12.8	8.05	9.54	0.37	0.15	2.97
3	Al ₃ Mn _{0.2} Zn _{0.3} Mg _{0.6} Si _{0.7}	62.5	4.2	14.6	6.3	12.5	8.59	10.19	0.37	0.13	2.86
4	Al ₃ Mn _{0.2} Zn _{0.3} Mg _{0.7} Si _{0.8}	60	4	16	6	14	9.02	10.71	0.38	0.12	2.82
5	Al _{3.5} Mn _{0.2} Zn _{0.7} Mg _{0.2} Si _{0.1}	74.5	4.3	2.1	14.9	4.3	4.09	5.67	6.06	0.41	3.39
6	Al ₄ Mn _{0.2} Zn _{0.8} Mg _{0.2} Si _{0.1}	75.5	3.8	1.9	15.1	3.8	4.29	5.94	5.43	0.38	3.41
7	Al ₄ Mn _{0.26} Zn _{0.9} Mg _{0.2} Si _{0.1}	73.3	4.8	1.8	16.5	3.7	4.51	6.1	4.88	0.38	3.57

**Figure 3.** Results of criteria multiobjective optimization for Al-Cu-Si-Zn-Mg system: (a) Λ versus Ω , (b) Λ versus density, and (c) $\Delta\chi_{\text{Allen}}$ versus density.

The resulted Al_{3.4}Cu_{0.5}Si_{0.2}Zn_{0.5}Mg_{0.2} phase diagram (Figure 5a) shows two different regions concerning the formation of hard intermetallic phases. Zn₂Mg and Al₂Cu based phases are in higher proportion below 316 °C and decrease significantly above this temperature. Presence of these compounds is determined by the high proportions of Zn, Mg, and Cu. At higher temperatures the BCC-A2 and FCC-A1 disordered phases form at approx. 488 °C through an invariant reaction from the liquid state. These structures were mentioned before in Cu and Si containing multicomponent alloys [33]. In the 316–488 °C range the alloy structure is composed mainly of disordered FCC-A1, BCC-A2 phases and multicomponent intermetallic Q-phase, which suggests that the alloy composition is favouring the complex structures at this temperature level. Modeling results show a near-equimolar composition of Al, Zn and Cu in the BCC-A2 phase and higher concentrations of Mg and Si in the Q-phase. The Al₂Cu phase is also forming with a steady increase in concentration, in this temperature range. The BCC-A2 and Q-phase structures become unstable at approx. 316 °C participating in a second invariant transformation with the formation of stable Zn₂Mg and Si-A4 phases. A substantial increase in the Al₂Cu phase is also presented after this critical transformation. The ductile FCC-A1 phase is predominant all across the temperature range. For the Al₃Mn_{0.2}Zn_{0.3}Mg_{0.7}Si_{0.8} alloy (Figure 5b), two

intermetallic phases of α - $\text{Al}_9\text{Mn}_2\text{Si}$ and Mg_2Si are shown to have great stability at lower and higher temperatures and form early during the solidification process. Same as in the previous alloy structure, the FCC_A1 phase is predominant at all temperatures, but starts forming after the intermetallic phases.

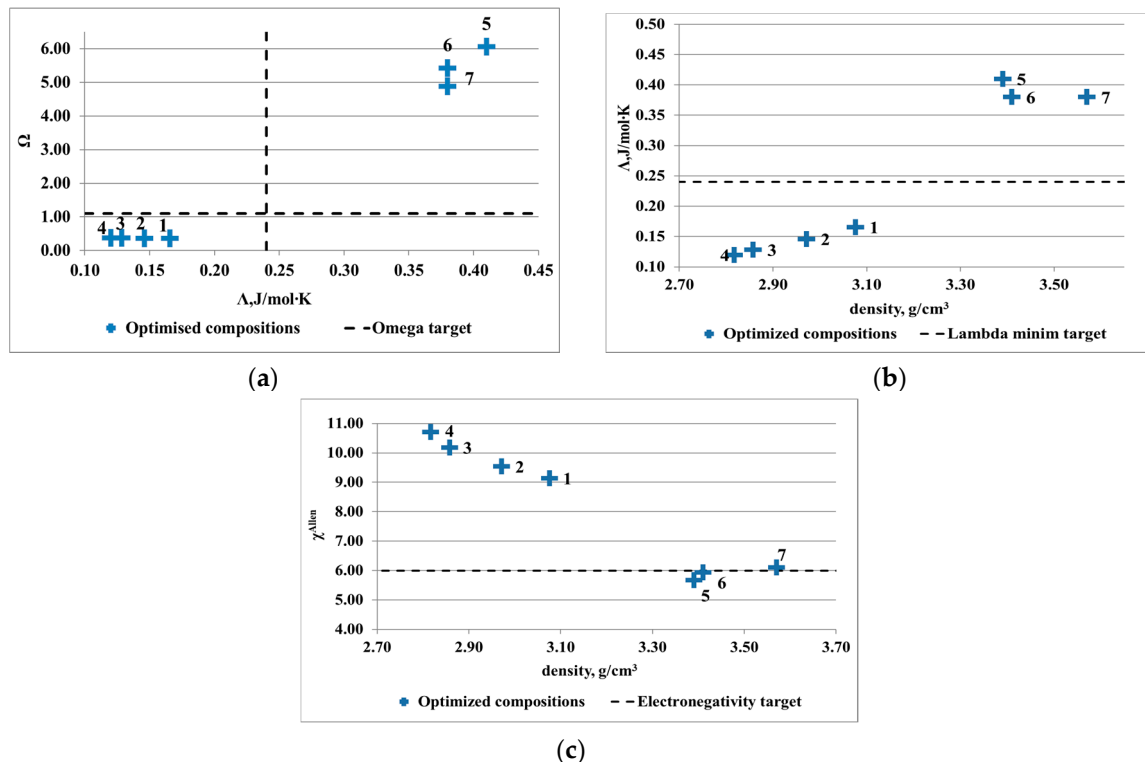


Figure 4. Results of criteria multiobjective optimization for Al-Mn-Zn-Mg-Si system: (a) Λ versus Ω , (b) Λ versus density, and (c) $\Delta\chi_{\text{Allen}}$ versus density.

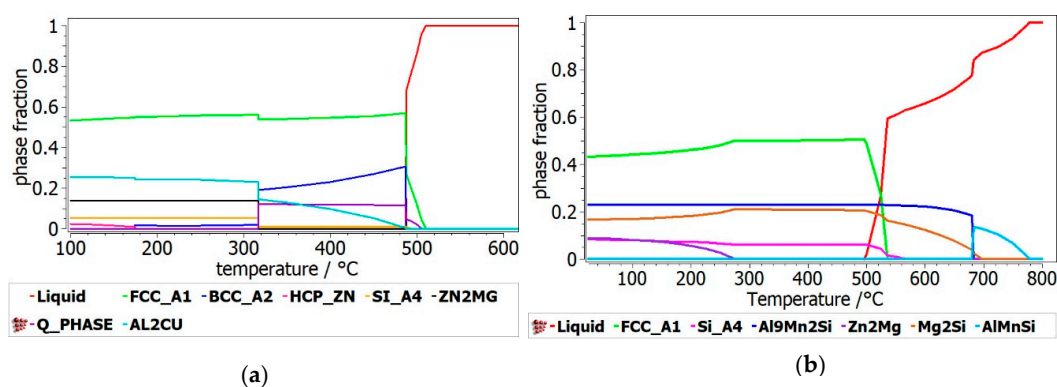


Figure 5. Phase composition versus temperature for the (a) $\text{Al}_{3.4}\text{Cu}_{0.5}\text{Si}_{0.2}\text{Zn}_{0.5}\text{Mg}_{0.2}$ and (b) $\text{Al}_3\text{Mn}_{0.2}\text{Zn}_{0.3}\text{Mg}_{0.7}\text{Si}_{0.8}$ alloys.

The phase evolution function of element concentration was also calculated for both alloy systems. In the Al-Cu-Si-Zn-Mg system (Figure 6), Cu content is critical for the formation of the Al_2Cu phase, with a peak at 40 wt.% where solid solutions are completely suppressed. A predominant BCC solid solution structure is found when Cu concentration is between 50 and 60 wt.%. The main influence of Zn content is shown by the transition between the FCC and BCC at higher Zn concentrations. The total proportion of the intermetallic based phases remains constant with the increase of Zn content, with the transition between the formation of Al_2Cu and Zn_2Mg phases.

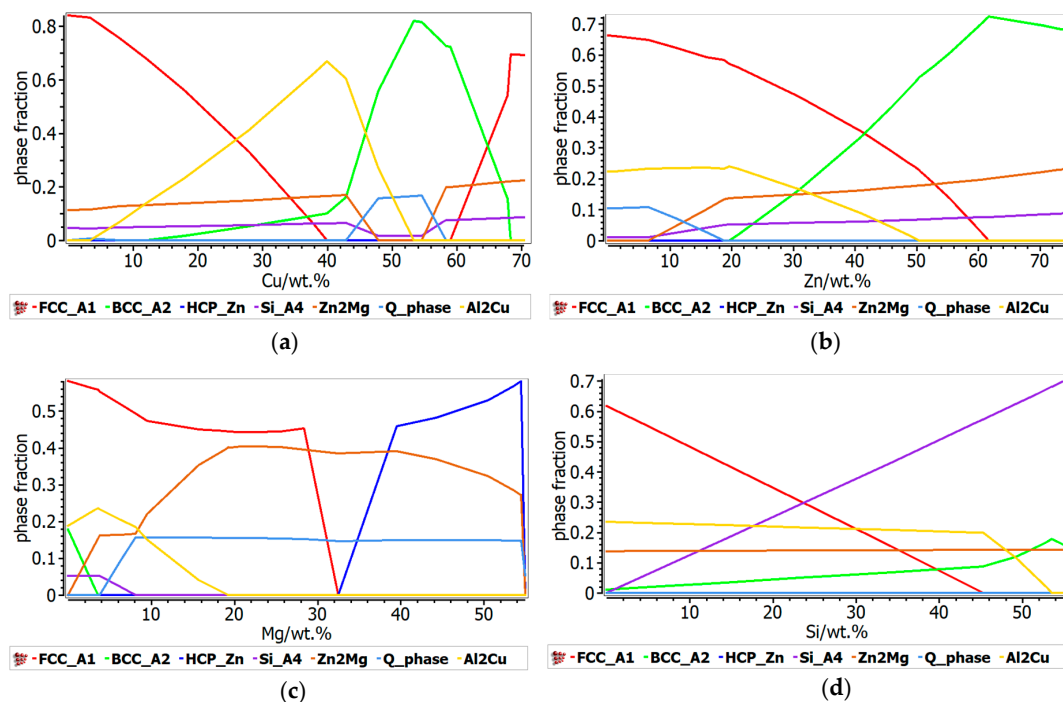


Figure 6. Influence of the element content over the phase stability in $\text{Al}_{3.4}\text{Cu}_{0.5}\text{Si}_{0.2}\text{Zn}_{0.5}\text{Mg}_{0.2}$: (a) Cu influence; (b) Zn influence; (c) Mg influence; (d) Si influence.

Higher concentrations of Mg have a strong influence over the formation of intermetallic based phases, mainly the Zn_2Mg intermetallic compound, which becomes very stable over 8 wt.% Mg. Because most of the Mg is taken for the formation of Zn_2Mg compound, the Si content does not influence the concentration of intermetallic based phases. The proportion of the FCC solid solution decreases with the increase of the Si content, which is typical for the Al-Si alloys.

The Al-Mn-Zn-Mg-Si alloy system (Figure 7) is mainly defined by the presence of Mn, which has an important contribution to the formation of complex compound-based phases. Thus, the increase of the Mn content induces a significant increase in the $\text{Al}_9\text{Mn}_2\text{Si}$ type- complex compound phase, which reaches a peak of 0.7 phase fraction at just 20 wt.% Mn, after which decreases abruptly at the exchange of the AlMnSi phase. Meanwhile, the proportion of FCC and BCC phases suffer a major decrease, with under 0.1 phase fraction at 20 wt.% Mn. Zn influence on the phase stability is similar to the Al-Cu-Si-Zn-Mg system, with the difference consisting in the formation of Mg_2Si phase instead of Al_2Cu phase. At lower Zn concentrations, Mg_2Si is more stable than Zn_2Mg . The FCC-A1 phase is decreasing strongly at the exchange of the BCC phase formation and the $\text{Al}_9\text{Mn}_2\text{Si}$ type phase is dominant at up to 55 wt.% Zn. As in the Al-Cu-Si-Zn-Mg system, the increase in Mg concentration determines a high increase on the intermetallic compounds proportion, thus the Mg_2Si compound is predominant after 20 wt.% Mg. As expected, the influence of Si content in the phase evolution of Al-Mn-Zn-Mg-Si structure is very similar to the Al-Cu-Si-Zn-Mg system.

The phases formed during non-equilibrium solidification, modeled with Scheil–Gulliver method, are shown in Figure 8. The behavior of the phases with termination S describes the cumulative solidification patterns, containing equilibrium and non-equilibrium values. The equilibrium and non-equilibrium solidification are similar for the $\text{Al}_3\text{Mn}_{0.2}\text{Zn}_{0.3}\text{Mg}_{0.7}\text{Si}_{0.8}$ alloy (Figure 8a), while in the $\text{Al}_{3.4}\text{Cu}_{0.5}\text{Si}_{0.2}\text{Zn}_{0.5}\text{Mg}_{0.2}$ alloy (Figure 8b) small differences are revealed between solidification temperatures. Obviously, the $\text{Al}_{3.4}\text{Cu}_{0.5}\text{Si}_{0.2}\text{Zn}_{0.5}\text{Mg}_{0.2}$ alloy presents a pattern characteristic to castable aluminum alloys, having also a smaller solidification temperature than $\text{Al}_3\text{Mn}_{0.2}\text{Zn}_{0.3}\text{Mg}_{0.7}\text{Si}_{0.8}$ (Figure 9). FCC-A1 type solid solution solidifies first in the $\text{Al}_{3.4}\text{Cu}_{0.5}\text{Si}_{0.2}\text{Zn}_{0.5}\text{Mg}_{0.2}$ alloy, while the solidification of $\text{Al}_3\text{Mn}_{0.2}\text{Zn}_{0.3}\text{Mg}_{0.7}\text{Si}_{0.8}$ alloy is mostly defined by the behavior of $\text{Al}_9\text{Mn}_2\text{Si}$ and

Mg₂Si intermetallic phases. The AlMnSi phase is unstable at lower temperatures and transforms into Al₉Mn₂Si at later stages.

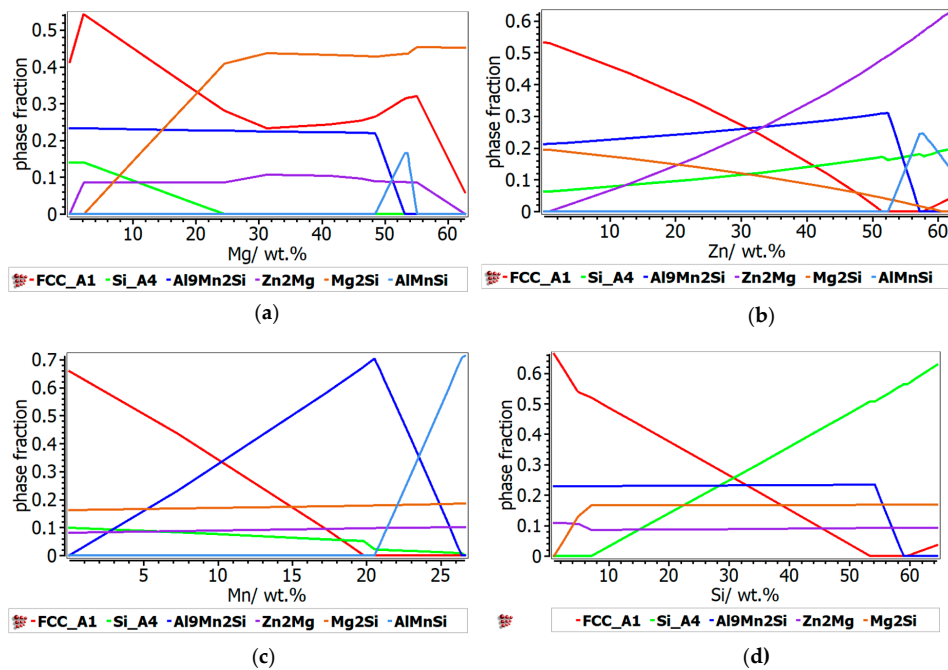


Figure 7. Influence of the element content over the phase stability in Al₃Mn_{0.2}Zn_{0.3}Mg_{0.7}Si_{0.8}: (a) Mg influence; (b) Zn influence; (c) Mn influence; (d) Si influence.

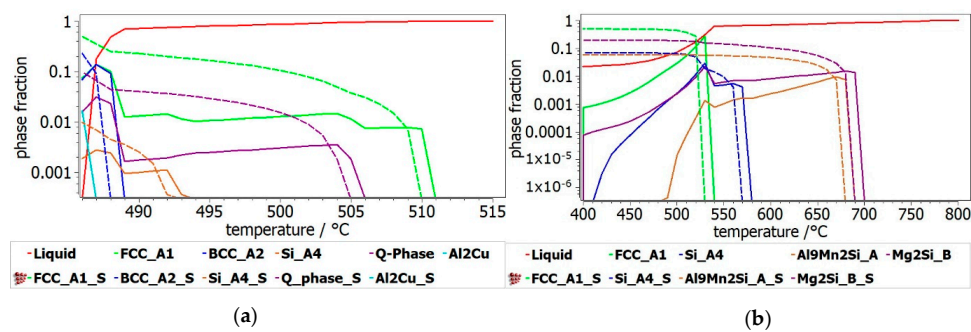


Figure 8. Scheil–Gulliver solidification diagrams for (a) Al_{3.4}Cu_{0.5}Si_{0.2}Zn_{0.5}Mg_{0.2} alloy and (b) Al₃Mn_{0.2}Zn_{0.3}Mg_{0.7}Si_{0.8} alloy.

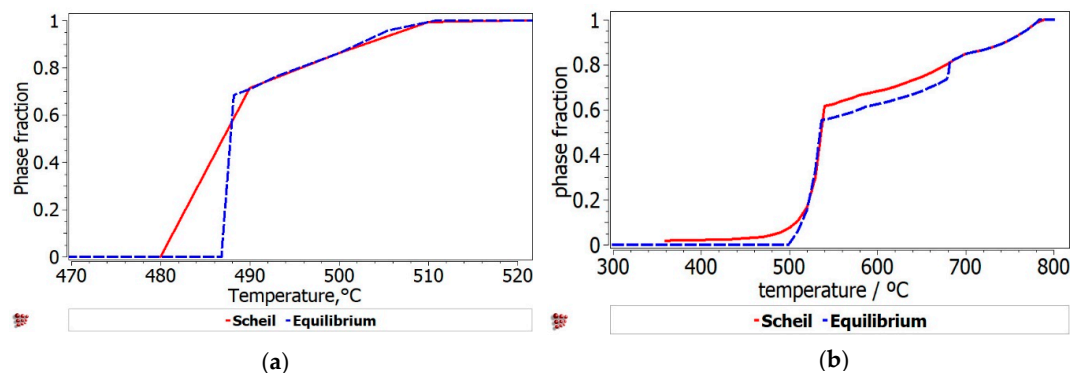


Figure 9. Equilibrium and Scheil–Gulliver liquidus solidification curves for the: (a) Al_{3.4}Cu_{0.5}Si_{0.2}Zn_{0.5}Mg_{0.2} alloy and (b) Al₃Mn_{0.2}Zn_{0.3}Mg_{0.7}Si_{0.8} alloy.

3.3. Kinetics Simulation

The heat treatment of $\text{Al}_{3.4}\text{Cu}_{0.5}\text{Si}_{0.2}\text{Zn}_{0.5}\text{Mg}_{0.2}$ and $\text{Al}_3\text{Mn}_{0.2}\text{Zn}_{0.3}\text{Mg}_{0.7}\text{Si}_{0.8}$ alloys was studied by the identification of hard phase precipitation in the FCC_A1 matrix. It can be seen from Figure 10 that the Al_2Cu precipitate has the highest fraction, while the precipitate radius is small and uniform across the annealing interval. The Q-phase is also shown in the $\text{Al}_{3.4}\text{Cu}_{0.5}\text{Si}_{0.2}\text{Zn}_{0.5}\text{Mg}_{0.2}$ precipitation diagram, but in lower proportion. The precipitation kinetics of the $\text{Al}_3\text{Mn}_{0.2}\text{Zn}_{0.3}\text{Mg}_{0.7}\text{Si}_{0.8}$ alloy (Figure 11) shows a close competition between the $\text{Al}_9\text{Mn}_2\text{Si}$ -type and Mg_2Si compounds. Nevertheless, the size of the complex compound is significantly smaller than that of the Mg_2Si . The Si_A4 phase is most likely found as eutectic in both alloys. Even if the AlMnSi precipitate is showing on the diagram, appears to be a nonequilibrium phase at 400 °C and is not stable during the heat treatment stage.

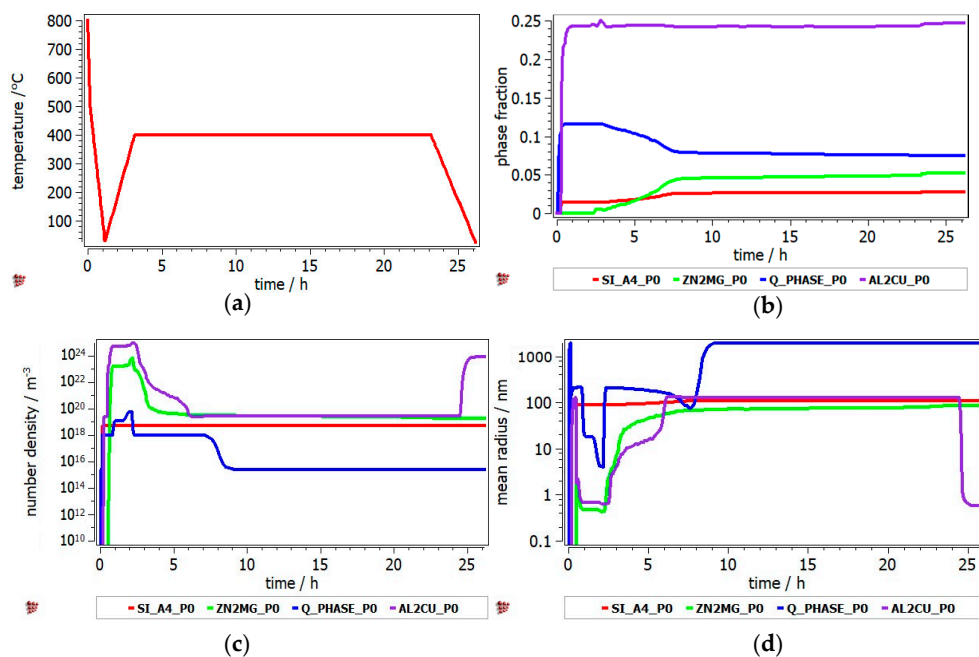


Figure 10. Precipitation kinetics in $\text{Al}_{3.4}\text{Cu}_{0.5}\text{Si}_{0.2}\text{Zn}_{0.5}\text{Mg}_{0.2}$ alloy during annealing at 400 °C, for 2 h: (a) heat treatment diagram, (b) precipitate phase fraction versus time, (c) precipitate number density versus time, (d) precipitate mean radius versus time.

3.4. Experimental Results

The experimental chemical composition of the alloys is presented in Table 4. The resulted alloy specimens have each element composition within a maximum of 2 wt.% interval from the nominal values. Due to the high percentage of the elements, a variation of 2 wt.% in composition has little influence on the structural behavior of the alloy, and the analyses implied in the paper has the meaning in offering a mainly qualitative and not standardized information related to the studied alloys characteristics.

Optical analyses of the alloy samples (Figures 12 and 13) revealed significantly different morphologies between as cast and heat-treated states. Optical microscopy results for the as cast $\text{Al}_{3.4}\text{Cu}_{0.5}\text{Si}_{0.2}\text{Zn}_{0.5}\text{Mg}_{0.2}$ alloys showed a fine and uniform dispersed dendritic structure (Figure 12a). Several phases are found in the interdendritic area, including occasional eutectic formations. The $\text{Al}_{3.4}\text{Cu}_{0.5}\text{Si}_{0.2}\text{Zn}_{0.5}\text{Mg}_{0.2}$ heat treated alloy (Figure 12b) shows a dendritic structure with several micropores, mainly placed in the interdendritic area. In average, less than 5 vol % porosity was found in the specimens. The dendrite size is significantly larger than in the as-cast alloy, with well-defined interdendritic phases. Eutectic formations were also identified in the heat-treated sample. The as-cast and heat treated $\text{Al}_3\text{Mn}_{0.2}\text{Zn}_{0.3}\text{Mg}_{0.7}\text{Si}_{0.8}$ samples (Figure 13a,b) show a similar fine dendritic structure.

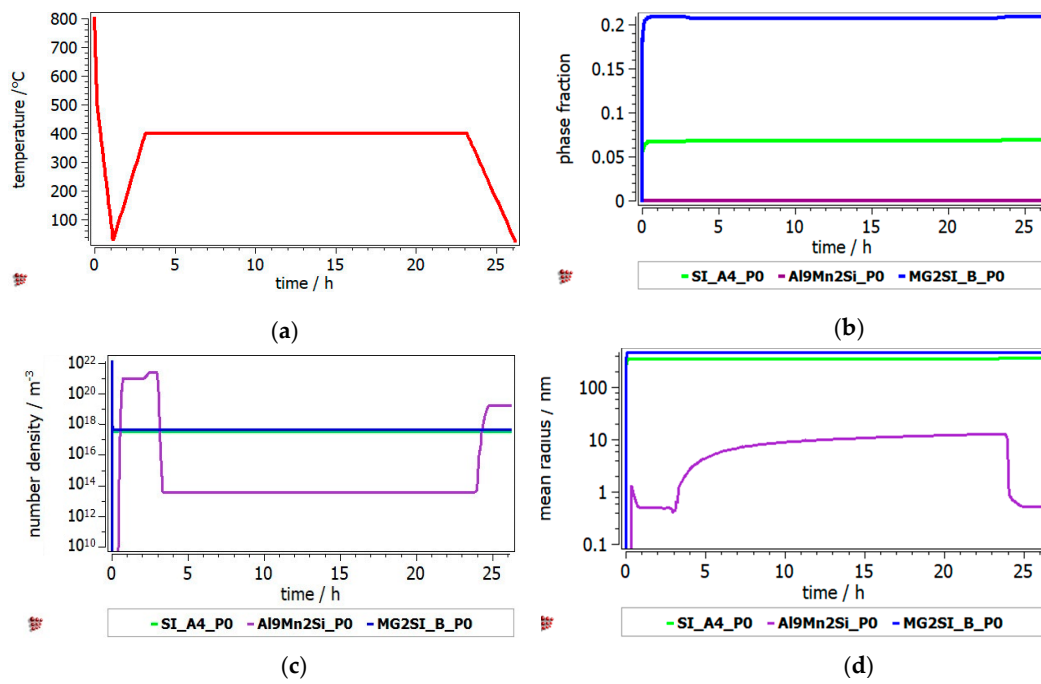


Figure 11. Precipitation kinetics in $Al_3Mn_{0.2}Zn_{0.3}Mg_{0.7}Si_{0.8}$ alloy during annealing at 400 °C, for 2 h: (a) heat treatment diagram, (b) precipitate phase fraction versus time, (c) precipitate number density versus time, (d) precipitate mean radius versus time.

Table 4. Alloys chemical composition in weight percent.

Alloy	Type	Al	Mg	Si	Zn	Cu	Mn
$Al_{3.4}Cu_{0.5}Si_{0.2}Zn_{0.5}Mg_{0.2}$	nominal	55	2.9	3.4	19.6	19	-
	actual	53.6	3.2	4.2	20.9	17.8	-
$Al_3Mn_{0.2}Zn_{0.3}Mg_{0.7}Si_{0.8}$	nominal	53.6	11.3	14.8	13	-	7.2
	actual	53.4	10.8	15.5	11.6	-	8.4

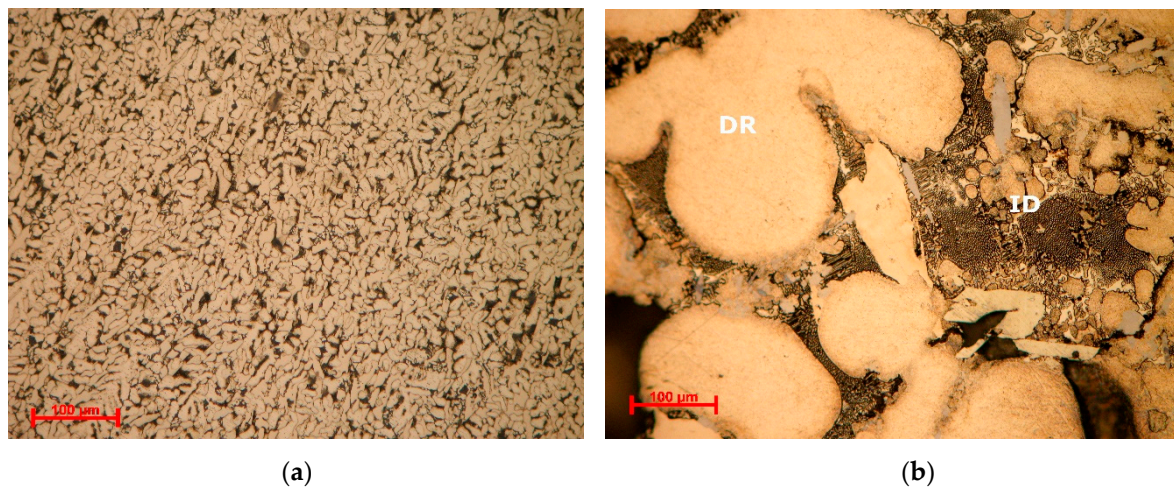


Figure 12. Optical micrographs of (a) as-cast and (b) annealed $Al_{3.4}Cu_{0.5}Si_{0.2}Zn_{0.5}Mg_{0.2}$ alloy. DR-dendritic area, ID-interdendritic area.

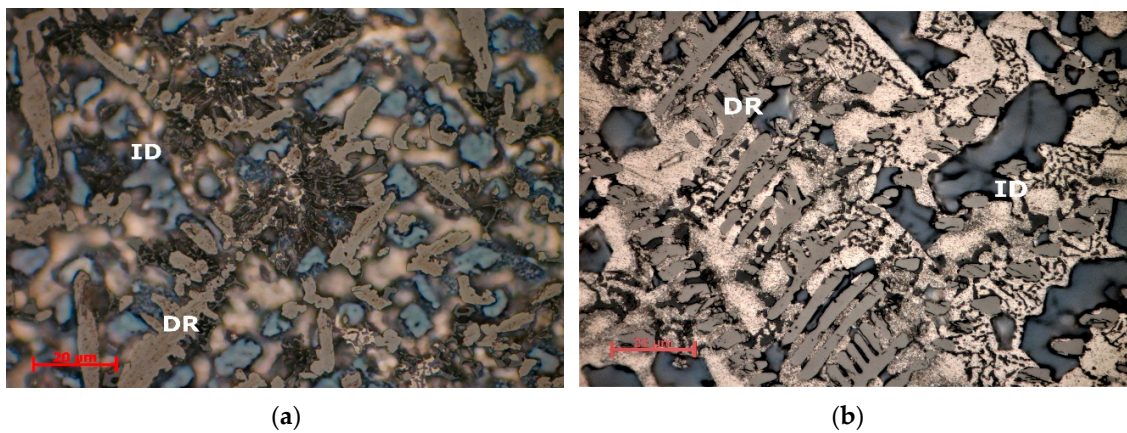


Figure 13. Optical micrographs of (a) as-cast and (b) annealed cast $\text{Al}_3\text{Mn}_{0.2}\text{Zn}_{0.3}\text{Mg}_{0.7}\text{Si}_{0.8}$ alloy. DR—dendritic area; ID—interdendritic area.

Well defined, but small dendrite secondary arms are present in the structures. Two different types of dendritic formations are identified. Micropores are present throughout both samples. Microporosity level was determined as 3 vol % from the analysed samples. Etching and higher magnification of the as-cast and heat treated $\text{Al}_3\text{Mn}_{0.2}\text{Zn}_{0.3}\text{Mg}_{0.7}\text{Si}_{0.8}$ alloy samples show a polyphasic interdendritic structure, with significant interdendritic eutectic. Hard intermetallic phases are present at similar sizes in both samples.

Microstructural analyses through scanning electron microscopy (Figures 14 and 15), shows large difference between the as-cast and heat-treated alloys. The as-cast $\text{Al}_{3.4}\text{Cu}_{0.5}\text{Si}_{0.2}\text{Zn}_{0.5}\text{Mg}_{0.2}$ (Figure 14a) is formed of multiple phases of similar size and uniform distribution in the material. After heat treatment the alloy exhibits a large dendrite structure and well-defined interdendritic eutectic (Figure 14b). The composition of $\text{Al}_{3.4}\text{Cu}_{0.5}\text{Si}_{0.2}\text{Zn}_{0.5}\text{Mg}_{0.2}$ phase structures, for as-cast and heat-treated states are presented in Table 5. Results for EDS analyses of $\text{Al}_{3.4}\text{Cu}_{0.5}\text{Si}_{0.2}\text{Zn}_{0.5}\text{Mg}_{0.2}$ alloy reveals high concentration of Al and Zn in the dendritic area (DR). Cu is found mainly in the interdendritic area (ID), forming well defined phases with Al, Zn, and Mg (ID1, ID2, ID3, ID4, and ID5). The eutectic formation investigated with EDS-mapping (Figures 16 and 17), is composed of Al and Zn based constituents. Mg and Si are found concentrated in common regions, most likely forming intermetallic compounds.

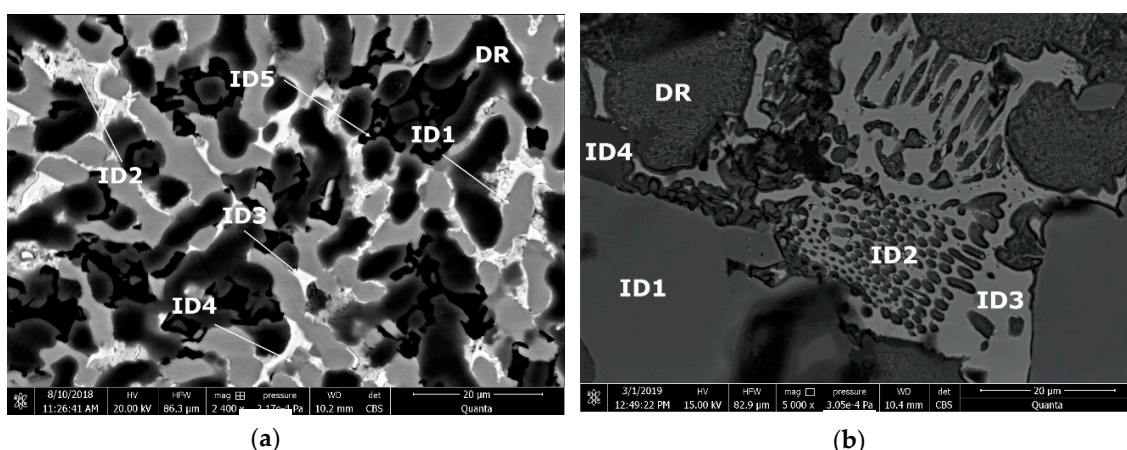


Figure 14. SEM images of (a) as-cast and (b) annealed cast $\text{Al}_{3.4}\text{Cu}_{0.5}\text{Si}_{0.2}\text{Zn}_{0.5}\text{Mg}_{0.2}$ alloy. DR—dendritic area; ID—interdendritic area; ID1,2,3, and 4—interdendritic phases (Table 4).

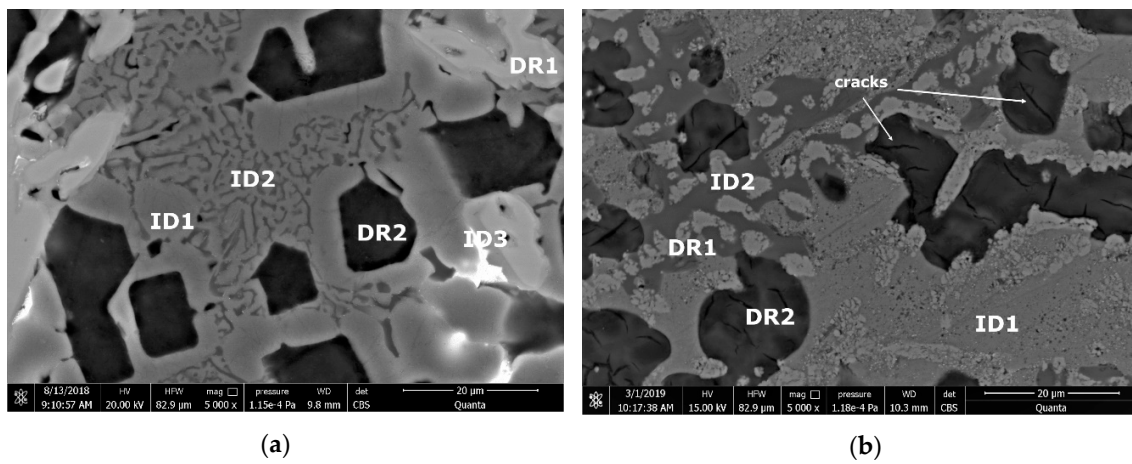


Figure 15. SEM images of (a) as-cast and (b) annealed cast $Al_3Mn_{0.2}Zn_{0.3}Mg_{0.7}Si_{0.8}$ alloy. DR—dendritic area; ID—interdendritic area; ID1,2,3, and 4—interdendritic phases (Table 5).

Table 5. EDS analyses results for $Al_{3.4}Cu_{0.5}Si_{0.2}Zn_{0.5}Mg_{0.2}$ alloy.

State	Phase	Composition, at %				
		Al	Cu	Si	Zn	Mg
as-cast	DR	90.22	2.32	-	7.46	-
	ID1	66.34	30.70	-	2.96	-
	ID2	48.55	3.68	-	44.55	3.22
	ID3	18.60	6.08	-	47.11	28.21
	ID4	2.74	0.71	32.23	2.06	62.26
	ID5	55.26	29.34	-	8.43	6.97
annealed	DR	89.45	-	-	10.55	-
	ID1	74.69	25.31	-	-	-
	ID2	22.29	8.96	-	66.34	2.41
	ID3	12.56	11.46	-	59.63	16.35
	ID4	4.23	8.54	30.15	2.62	54.46

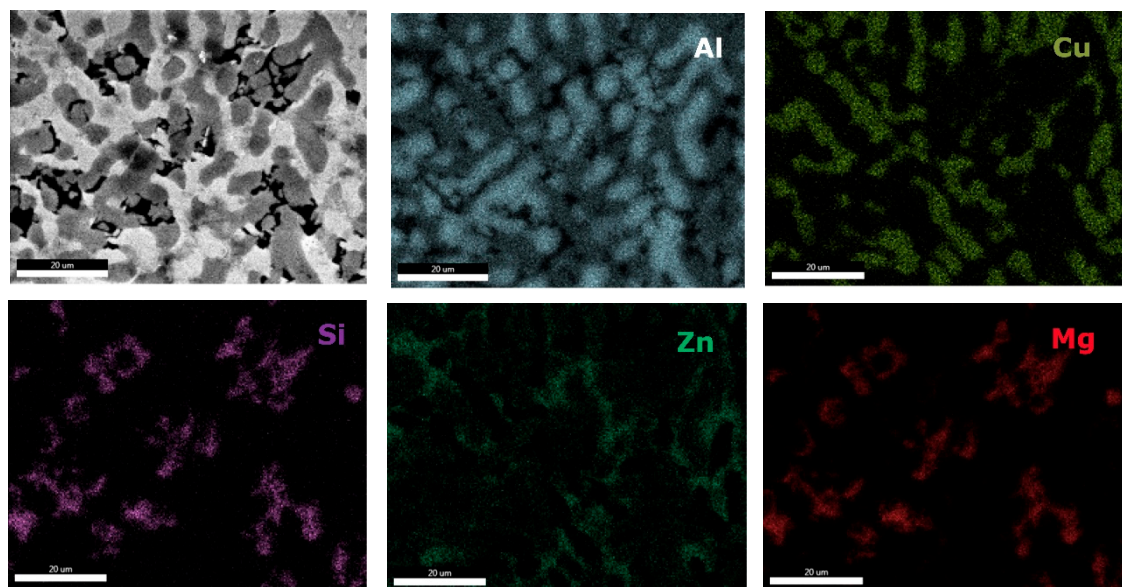


Figure 16. EDS mapping of as-cast $Al_{3.4}Cu_{0.5}Si_{0.2}Zn_{0.5}Mg_{0.2}$ alloy.

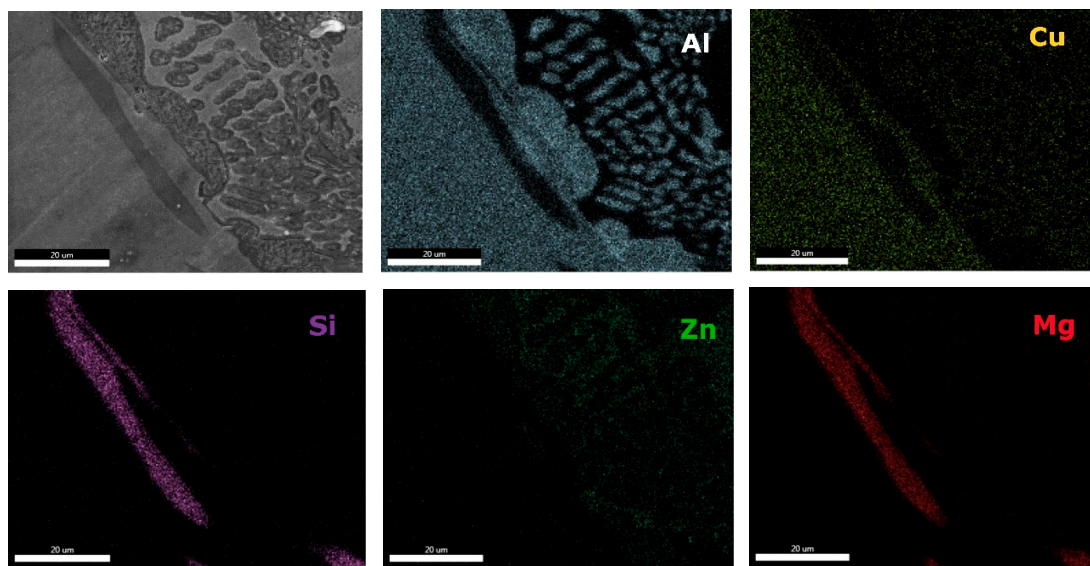


Figure 17. EDS mapping of heat treated $\text{Al}_{3.4}\text{Cu}_{0.5}\text{Si}_{0.2}\text{Zn}_{0.5}\text{Mg}_{0.2}$ alloy.

The as cast and heat-treated structures for $\text{Al}_3\text{Mn}_{0.2}\text{Zn}_{0.3}\text{Mg}_{0.7}\text{Si}_{0.8}$ alloy (Figure 15) show similar phase sizes with small differences related to the distribution of interdendritic eutectic formations. Dark intermetallic phases with dendritic appearance are well distinguished at high magnifications, presenting small internal cracks in the heat-treated sample.

The interdendritic area indicates differences in terms of phase size and distribution, both samples revealing multiple phases. Phase composition determined by EDS analysis (Table 6) showed Al-Mn and Mg-Si based dendritic formations. Three separate interdendritic phases, with various concentrations of the elements (ID1, ID2, and ID3), were distinguished in the as-cast sample. Al is present in larger quantity in the interdendritic area forming a continuous phase with Zn. An occasional phase composed of Al, Mn, Si, and Zn was also identified in the as-cast sample. Si was also identified segregated in the interdendritic area. Similar compositions were found in the heat-treated sample, setting aside a minor phase with large Zn concentration. The EDS-mapping results (Figures 18 and 19) confirm the previous findings. The well-dispersed hard phases are composed mostly of Si and Mg. Si segregations appear as long branches in certain regions. Al and Mn are found highly concentrated in the dendritic area.

Table 6. EDS analyses results for $\text{Al}_3\text{Mn}_{0.2}\text{Zn}_{0.3}\text{Mg}_{0.7}\text{Si}_{0.8}$ alloy.

State	Phase	Composition, at %				
		Al	Mn	Si	Zn	Mg
as-cast	DR1	63.30	22.25	12.09	2.36	-
	DR2	6.87	4.88	29.78	1.30	57.17
	ID1	90.84	-	1.46	6.10	1.60
	ID2	20.61	-	75.31	4.08	-
	ID3	55.04	6.77	4.56	29.92	3.71
annealed	DR1	67.56	20.09	12.07	0.28	-
	DR2	1.85	-	37.54	0.89	59.72
	ID1	89.59	-	0.45	8.99	0.97
	ID2	8.23	5.12	83.01	2.73	0.91

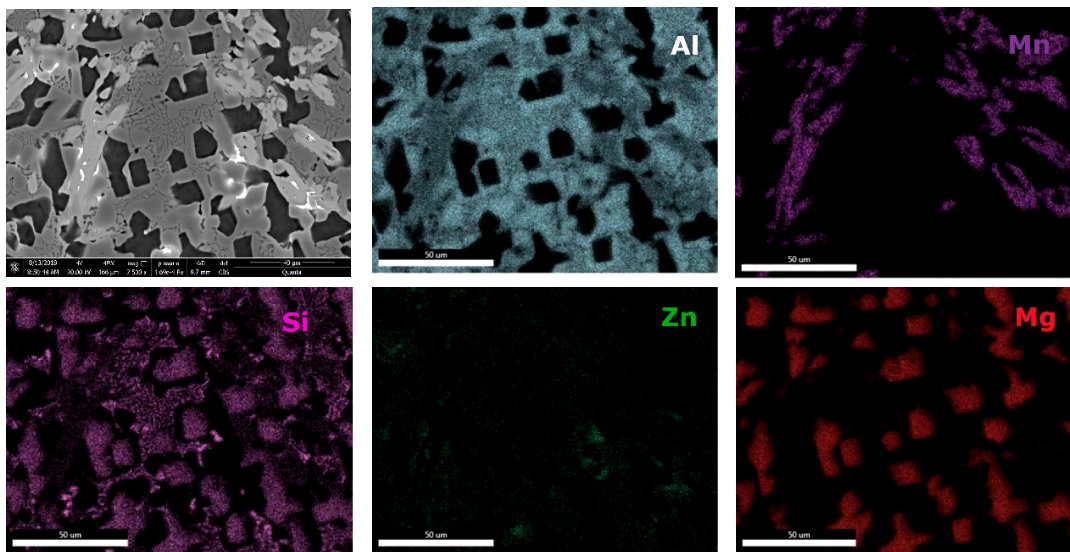


Figure 18. EDS mapping of as-cast $\text{Al}_3\text{Mn}_{0.2}\text{Zn}_{0.3}\text{Mg}_{0.7}\text{Si}_{0.8}$ alloy.

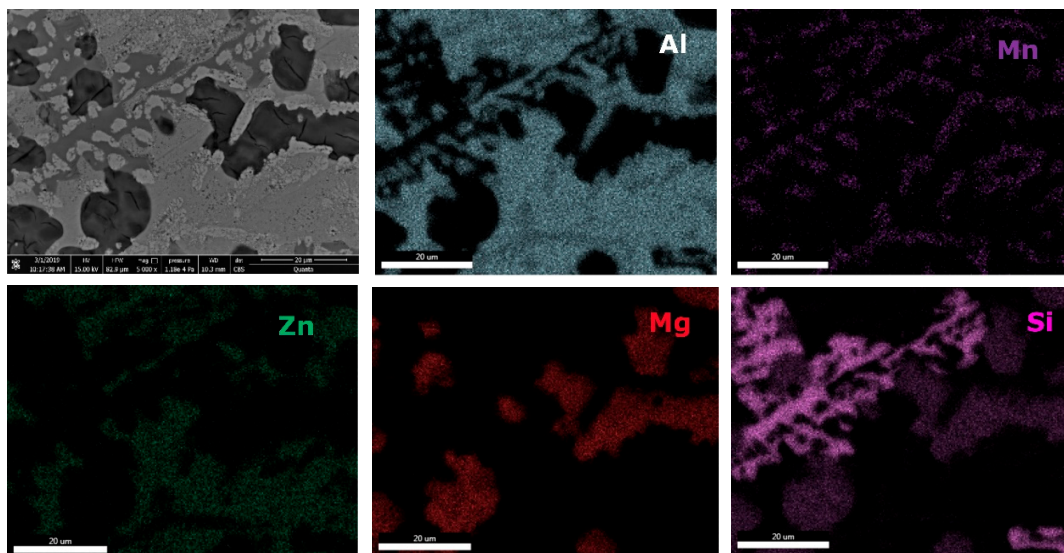


Figure 19. EDS mapping of heat treated $\text{Al}_3\text{Mn}_{0.2}\text{Zn}_{0.3}\text{Mg}_{0.7}\text{Si}_{0.8}$ alloy.

The X-ray analysis of the as-cast $\text{Al}_{3.4}\text{Cu}_{0.5}\text{Si}_{0.2}\text{Zn}_{0.5}\text{Mg}_{0.2}$ alloy (Figure 20) indicates a structure composed of Al and Zn based solid solutions and Al_2Cu , $\text{Mg}_2\text{Zn}_{11}$, Mg_2Si , MgZn_2 intermetallic compound-based phases. Phase proportion calculations revealed a high content of FCC-A1 (Al) solid solution (48 wt.%) and Al_2Cu -C16 phase (34 wt.%). The HCP-A3 (Zn) solid solution (8 wt.%), Z phase of type $(\text{Cu}_6\text{Mg}_2\text{Al}_5)\text{Mg}_2\text{Zn}_{11}$ (4 wt.%), M phase of type $(\text{CuMgAl})\text{MgZn}_2$ (4 wt.%) and MgSi_2 (2 wt.%) have minority proportions. After the heat treatment performed at 400 °C for 20 h, it can be noted that the hexagonal phase M (a quaternary continuous solid solution, formed between the ternary compound CuMgAl and the binary compound MgZn_2) is no longer present in the alloy structure and the cubic phase Z (a quaternary continuous solid solution, between the ternary compound $\text{Cu}_6\text{Mg}_2\text{Al}_5$ and the binary compound $\text{Mg}_2\text{Zn}_{11}$) increases in concentration. In the heat-treated sample, small percentage changes of the FCC-A1 type (50 wt.%) and Al_2Cu -C16 type (31 wt.%) phases are also observed, while Mg_2Si decreases significantly (1.7 wt.%).

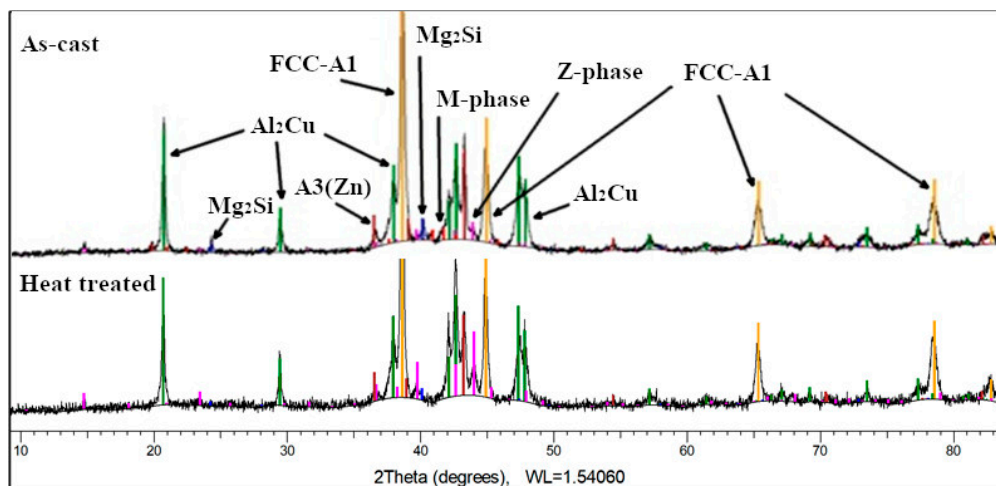


Figure 20. XRD results for as-cast and heat treated $\text{Al}_{3.4}\text{Cu}_{0.5}\text{Si}_{0.2}\text{Zn}_{0.5}\text{Mg}_{0.2}$ alloy.

The as-cast $\text{Al}_3\text{Mn}_{0.2}\text{Zn}_{0.3}\text{Mg}_{0.7}\text{Si}_{0.8}$ alloy structure (Figure 21) consists of solid solutions and intermetallic compound phases. The FCC-Al (Al) type solid solution is predominant (55 wt.%), while $\text{Al}_{4.01}\text{MnSi}_{0.74}$ (16 wt.%), $\text{Al}_{10}(\text{Mn}_{0.58}\text{Zn}_{0.24}\text{Si}_{0.18})_3$ (10 wt.%), and Mg_2Si (13 wt.%) intermetallics are in much less proportions. Si was found also at 6 wt.%. The $\text{Al}_{10}(\text{Mn}_{0.58}\text{Zn}_{0.24}\text{Si}_{0.18})_3$ is a hexagonal complex phase formed from the binary compound $\text{Al}_{10}\text{Mn}_3$ and the ternary compound $(\text{Al}_9\text{Si})\text{Mn}_3$. The diffraction spectrum for the heat treated $\text{Al}_3\text{Mn}_{0.2}\text{Zn}_{0.3}\text{Mg}_{0.7}\text{Si}_{0.8}$ alloy indicates a four-phase composition. The $\text{Al}_{10}(\text{Mn}_{0.58}\text{Zn}_{0.24}\text{Si}_{0.18})_3$ phase is no longer present which contributes to the increase of $\text{Al}_{4.01}\text{MnSi}_{0.74}$ (32 wt.%) and Mg_2Si (16 wt.%) phases, at the expense of FCC-Al phase (46 wt.%).

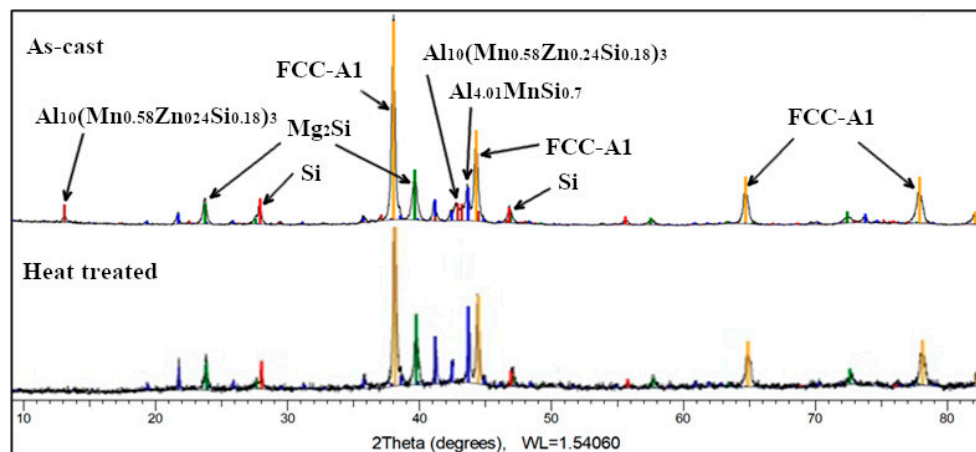


Figure 21. XRD results for as-cast and heat treated $\text{Al}_3\text{Mn}_{0.2}\text{Zn}_{0.3}\text{Mg}_{0.7}\text{Si}_{0.8}$ alloy.

The mechanical testing results for both alloys in as-cast and heat treated states are presented in Table 7, Figures 22 and 23. The $\text{Al}_{3.4}\text{Cu}_{0.5}\text{Si}_{0.2}\text{Zn}_{0.5}\text{Mg}_{0.2}$ alloy presented a slightly higher resistance (590 MPa in as-cast and 618 MPa in heat treated state) than the $\text{Al}_3\text{Mn}_{0.2}\text{Zn}_{0.3}\text{Mg}_{0.7}\text{Si}_{0.8}$ alloy (486 MPa in as-cast and 507 MPa in heat treated state).

Both alloys showed a brittle behavior with elongation under 3%. The microhardness tests showed high values in comparison with the conventional aluminum alloys (A357.0 and A5083). The as-cast samples presented a fine and well distributed phase structure, which allowed for multiple determinations with similar values, averaged at 268 HV for $\text{Al}_{3.4}\text{Cu}_{0.5}\text{Si}_{0.2}\text{Zn}_{0.5}\text{Mg}_{0.2}$ alloy and at 277 HV for the $\text{Al}_3\text{Mn}_{0.2}\text{Zn}_{0.3}\text{Mg}_{0.7}\text{Si}_{0.8}$ alloy. However, the annealed structures presented large and well-defined phases, so microhardness indentations revealed individual values for each distinct phase. The rounded proportional average of the determined values for the annealed alloys were: 274 HV

for $\text{Al}_{3.4}\text{Cu}_{0.5}\text{Si}_{0.2}\text{Zn}_{0.5}\text{Mg}_{0.2}$ and 283 HV for $\text{Al}_3\text{Mn}_{0.2}\text{Zn}_{0.3}\text{Mg}_{0.7}\text{Si}_{0.8}$. The results showed similar microhardness values between the two alloy states.

Table 7. Alloys chemical composition in weight percent.

Alloy	State	Compression Yield Strength, (MPa)	Hardness, (HV)
$\text{Al}_{3.4}\text{Cu}_{0.5}\text{Si}_{0.2}\text{Zn}_{0.5}\text{Mg}_{0.2}$	as-cast	590	268
	annealed	618	274
$\text{Al}_3\text{Mn}_{0.2}\text{Zn}_{0.3}\text{Mg}_{0.7}\text{Si}_{0.8}$	as-cast	486	277
	annealed	507	283
A357.0	as-cast	240	120
AA5083	wrought	380	80

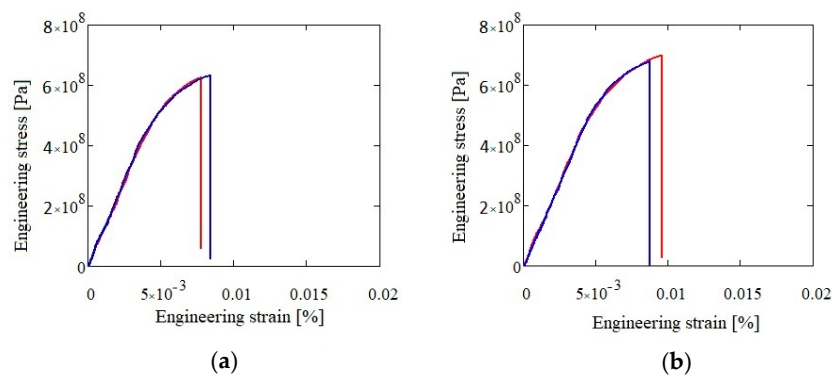


Figure 22. Compression test results for as-cast (a) and heat treated (b) $\text{Al}_{3.4}\text{Cu}_{0.5}\text{Si}_{0.2}\text{Zn}_{0.5}\text{Mg}_{0.2}$ alloy.

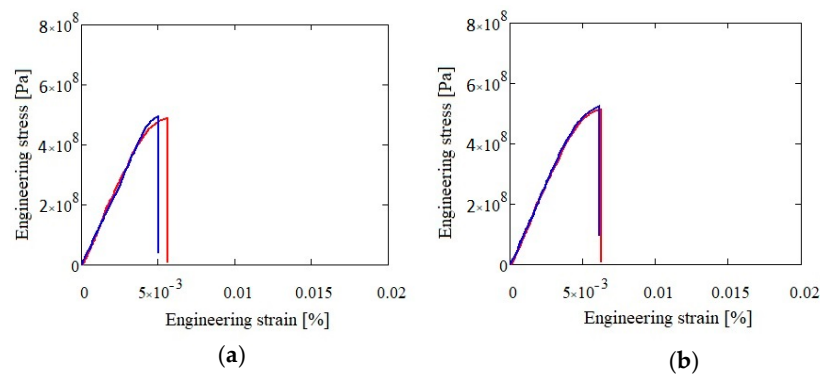


Figure 23. Compression test results for as-cast (a) and heat treated (b) $\text{Al}_3\text{Mn}_{0.2}\text{Zn}_{0.3}\text{Mg}_{0.7}\text{Si}_{0.8}$ alloy.

4. Discussion

The thermodynamic and Hume-Rothery rules for the formation of solid solution structures offer a good estimate for the selection of most appropriate compositions, but cannot fully predict real life experimental results. The targeted alloys were intentionally annealed to eliminate inherent out of equilibrium structures that may appear after the casting process.

Selection criteria applied to the $\text{Al}_{3.4}\text{Cu}_{0.5}\text{Si}_{0.2}\text{Zn}_{0.5}\text{Mg}_{0.2}$ alloy showed optimal values for most of the parameters. The electronegativity difference was the only parameter that was above the recommended limit. By comparison, the selected $\text{Al}_3\text{Mn}_{0.2}\text{Zn}_{0.3}\text{Mg}_{0.7}\text{Si}_{0.8}$ alloy presented most of the criteria parameters out of the recommended limits, which suggests a structure with a higher percentage of intermetallic compounds. For both alloys, the experimental findings matched the criteria calculations and showed a high percentage of the FCC-Al phase and presence of intermetallic compounds. For the $\text{Al}_3\text{Mn}_{0.2}\text{Zn}_{0.3}\text{Mg}_{0.7}\text{Si}_{0.8}$ alloy was found a significantly larger number of intermetallic phases.

CALPHAD method produced similar phase configurations with those obtained in the experimental results, with slight changes for low proportion phases. Thus, Si suggested by MatCalc was not found in the $\text{Al}_{3.4}\text{Cu}_{0.5}\text{Si}_{0.2}\text{Zn}_{0.5}\text{Mg}_{0.2}$ heat treated sample, instead $\text{Mg}_2\text{Zn}_{11}$ was detected at X-ray analysis. The Q-phase was determined as a stable phase in the studied alloy and was not indicated by the analyses of the experimental samples. Thermodynamic calculations showed presence of Zn_2Mg which were not detected in the $\text{Al}_3\text{Mn}_{0.2}\text{Zn}_{0.3}\text{Mg}_{0.7}\text{Si}_{0.8}$ heat treated sample. The $\text{Al}_9\text{Mn}_2\text{Si}$ phase shown in MatCalc simulation is very similar to the experimental $\text{Al}_{4.01}\text{MnSi}_{0.74}$. It is known that the stoichiometry of the $\text{Al}_{4.01}\text{MnSi}_{0.74}$ phase is similar to the stoichiometry of the $\alpha\text{-Al}_9\text{Mn}_2\text{Si}$ phase, thus indicating a similar crystal structure [34]. The proportion of phases was also well represented by the CALPHAD method.

There is also a good representation of the solidification behavior of the selected alloys obtained with the Scheil–Gulliver method. The resulted diagram for $\text{Al}_{3.4}\text{Cu}_{0.5}\text{Si}_{0.2}\text{Zn}_{0.5}\text{Mg}_{0.2}$ alloy (Figure 8a) showed that the first phase to form is FCC-A1, which is indicated as a dendrite formation in the optical and SEM results. The $\text{Al}_3\text{Mn}_{0.2}\text{Zn}_{0.3}\text{Mg}_{0.7}\text{Si}_{0.8}$ alloy has a more complex structure with two dendrite formations (Mg_2Si and $\text{Al}_9\text{Mn}_2\text{Si}$), which are also indicated by the solidification simulation diagram (Figure 8b).

Precipitation kinetics was applied to determine the structural changes in the as-cast structure over the annealing process. MatCalc software was setup to predict the nucleation and growth of the precipitated intermetallic phases during the heat treatment process, starting with the as-cast structure. The simulation results for $\text{Al}_{3.4}\text{Cu}_{0.5}\text{Si}_{0.2}\text{Zn}_{0.5}\text{Mg}_{0.2}$ alloy indicated a high proportion of the Al_2Cu precipitate, which was maintained at the same value from the as-cast structure. The results were verified by X-ray analyses. The number density of Al_2Cu decreases from as-cast to heat treated state, which remains consistent with the increase in the precipitate size, shown both by the simulation and SEM results. However, the size of the precipitate is much larger in the experimental specimens. The simulation results for the $\text{Al}_3\text{Mn}_{0.2}\text{Zn}_{0.3}\text{Mg}_{0.7}\text{Si}_{0.8}$ shows important discrepancies against the experimental findings. The Mg_2Si precipitate is in much larger proportion than the $\text{Al}_9\text{Mn}_2\text{Si}$ precipitate in the MatCalc simulation, which is in contradiction with the X-ray analyses results. Still, there are similarities regarding the high stability of the Mg_2Si precipitate number density and size, which can be observed from the simulation and microstructural characterization images.

The SEM-EDS and XRD results show a larger number of phases for the as-cast specimens. The complex M phase in $\text{Al}_{3.4}\text{Cu}_{0.5}\text{Si}_{0.2}\text{Zn}_{0.5}\text{Mg}_{0.2}$ and complex phase $\text{Al}_{10}(\text{Mn}_{0.58}\text{Zn}_{0.24}\text{Si}_{0.18})_3$ in $\text{Al}_3\text{Mn}_{0.2}\text{Zn}_{0.3}\text{Mg}_{0.7}\text{Si}_{0.8}$ are no longer present in the annealed state. This illustrates the metastable structure that is present in the as-cast samples and that slow diffusion processes are taking place in complex concentrated alloys. There is also a large difference between the behavior of the selected alloys during the annealing process. The $\text{Al}_{3.4}\text{Cu}_{0.5}\text{Si}_{0.2}\text{Zn}_{0.5}\text{Mg}_{0.2}$ alloy suffers large transformations in phase size and distribution, similar to the castable aluminum alloys, while the $\text{Al}_3\text{Mn}_{0.2}\text{Zn}_{0.3}\text{Mg}_{0.7}\text{Si}_{0.8}$ presents small changes in structural configuration, similar to the wrought aluminum alloys.

The mechanical properties of the alloys showed relatively high values for compression yield strength and hardness, in comparison with conventional aluminum alloys. This was expected due to the higher content of intermetallic phases. Unfortunately, the stress strain curves showed a brittle behavior that is detrimental for practical use. Even if the structural change is significant after annealing, with a significantly larger grain size, the $\text{Al}_{3.4}\text{Cu}_{0.5}\text{Si}_{0.2}\text{Zn}_{0.5}\text{Mg}_{0.2}$ retains similar values for the mechanical properties. This aspect could be analysed further in future studies. The $\text{Al}_3\text{Mn}_{0.2}\text{Zn}_{0.3}\text{Mg}_{0.7}\text{Si}_{0.8}$ alloy presents no significant changes in grain size after annealing (typical to wrought alloys) and consequently the mechanical properties present similar values for both alloy states.

Overall, the tools used for the prediction of the lightweight CCAs structures were in good agreement with the experimental findings. Small differences shown between simulation and experimental results indicate inherent errors that may appear when calculating multicomponent alloys with a large proportion of elements. Elemental diffusion plays an important role in the evolution of the alloys

structure, leading to the formation of complex phases, which are hard to be determined by conventional analysis methods and also difficult to be simulated by present software.

The selected compositions show a good potential for obtaining practical, low cost LWCCA, with improved properties. The substantial increase in the alloy's elements composition does not show dramatical changes in the structural behaviors. The intermetallic phases induced by the higher composition of the reactive elements, typical for LWCCA, are not necessarily detrimental to the final properties. A uniform distribution and reduced size of the precipitates can lead to a stable structure with high mechanical properties at higher operation temperatures. However, future studies are recommended for further compositional tuning and customised heat treatment processes to obtain optimal configurations for targeted applications.

5. Conclusions

The selection and analyses of low weight complex concentrated alloys, with common and less expensive elements, before and after heat treatment, were presented in the paper. The selection of alloys with low density and high solid solution content from Al-Cu-Si-Zn-Mg and Al-Mn-Zn-Mg-Si systems was achieved by the optimization of previously established semiempirical criteria. Results showed that a high aluminum content determined better solid solution forming ability for both alloy systems. While Cu, Zn, and Mn have a beneficial influence on the criteria parameters, the increase in element content affects the density of the alloy. A balance between density and criteria optimal values, modeled with an optimization software, was applied to offer practical solutions in the selection process.

The selected $\text{Al}_{3.4}\text{Cu}_{0.5}\text{Si}_{0.2}\text{Zn}_{0.5}\text{Mg}_{0.2}$ and $\text{Al}_3\text{Mn}_{0.2}\text{Zn}_{0.3}\text{Mg}_{0.7}\text{Si}_{0.8}$ alloys were analysed for structural behavior by CALPHAD, solidification and kinetics simulations. Phase diagrams showed the formation of a multiphase structure with preponderant solid solutions. Intermetallic compound-based phases were found at lower concentrations but still significantly higher than in the conventional aluminum alloys. Two invariant transformations were indicated for $\text{Al}_{3.4}\text{Cu}_{0.5}\text{Si}_{0.2}\text{Zn}_{0.5}\text{Mg}_{0.2}$ alloy, with a BCC-A2 phase stable between 316–488 °C. The influence of the elements on the structural evolution were similar with the results obtained from semiempirical criteria calculations. The non-equilibrium solidification simulation discussed the order of which the phases are solidifying in normal casting conditions. The soft FCC phase is stabilizing first in the $\text{Al}_{3.4}\text{Cu}_{0.5}\text{Si}_{0.2}\text{Zn}_{0.5}\text{Mg}_{0.2}$ alloy, while intermetallic compound phases Mg_2Si and $\text{Al}_9\text{Mn}_2\text{Si}$ are forming first in the $\text{Al}_3\text{Mn}_{0.2}\text{Zn}_{0.3}\text{Mg}_{0.7}\text{Si}_{0.8}$ alloy. The diffusion driven precipitation simulation offered indications on the formation of intermetallic precipitates in the solid solution matrix, showing that the Al_2Cu and Mg_2Si phases will be stabilizing at highest concentration levels for the $\text{Al}_{3.4}\text{Cu}_{0.5}\text{Si}_{0.2}\text{Zn}_{0.5}\text{Mg}_{0.2}$ and $\text{Al}_3\text{Mn}_{0.2}\text{Zn}_{0.3}\text{Mg}_{0.7}\text{Si}_{0.8}$ alloys, respectively.

The experimental findings, provided by optical, SEM-EDS, and XRD analyses, indicated that both alloys presented complex structures, containing mostly solid solutions, but also a significant amount of intermetallic phases. The $\text{Al}_{3.4}\text{Cu}_{0.5}\text{Si}_{0.2}\text{Zn}_{0.5}\text{Mg}_{0.2}$ presented a refined structure in the as-cast state with a predominant Al solid solution phase. The Al_2Cu and Mg-Zn intermetallics were also present in the alloy structure and continued to remain at a high percentage in the heat-treated samples. A dendritic structure based on FCC-Al phase was indicated in the $\text{Al}_{3.4}\text{Cu}_{0.5}\text{Si}_{0.2}\text{Zn}_{0.5}\text{Mg}_{0.2}$ alloy. The $\text{Al}_3\text{Mn}_{0.2}\text{Zn}_{0.3}\text{Mg}_{0.7}\text{Si}_{0.8}$ alloy showed a refined structure that was maintained also after the annealing process. This time the dendritic formations were indicated to be intermetallic compound phases: Mg_2Si and $\text{Al}_{4.01}\text{MnSi}_{0.74}$. Between the as-cast and heat-treated state, a transformation of less stable $\text{Al}_{10}(\text{Mn}_{0.58}\text{Zn}_{0.24}\text{Si}_{0.18})_3$ into $\text{Al}_{4.01}\text{MnSi}_{0.74}$ was revealed, which lead to a significant increase in the concentration of the $\text{Al}_{4.01}\text{MnSi}_{0.74}$ compound (32 wt.%). The mechanical characterisation of the alloys revealed a high compression strength for both alloys (aprox 600 Mpa for $\text{Al}_{3.4}\text{Cu}_{0.5}\text{Si}_{0.2}\text{Zn}_{0.5}\text{Mg}_{0.2}$ and aprox. 500 MPa for $\text{Al}_3\text{Mn}_{0.2}\text{Zn}_{0.3}\text{Mg}_{0.7}\text{Si}_{0.8}$) and brittle behavior. The microhardness was found in the range of hard aluminum alloys (250–300 HV).

The comparison of the experimental results with the criteria and simulation results showed good representations. There were small differences in phase composition and precipitation behavior between

the CALPHAD equilibrium diagrams for both alloys, kinetics simulation, and experimental results for the $\text{Al}_3\text{Mn}_{0.2}\text{Zn}_{0.3}\text{Mg}_{0.7}\text{Si}_{0.8}$ alloy. These relative inconsistencies could be resolved in the future development of the software by improving the alloys database and the diffusion simulation, which are difficult to achieve for multicomponent alloys with reactive elements.

The intention of this study was to provide a path in the selection of multicomponent CCAs, containing less expensive raw materials, for lightweight applications, using tools that are readily available. The optimization criteria can be easily modified to fit required properties. The alloying examples presented in the paper were studied from several angles to give an indication of the expected structural behavior in this type of alloys.

Author Contributions: Conceptualization, D.M. and I.C.B.; Methodology, M.T.O.; Software, D.M. and B.A.S.; Validation, V.G., D.V., and M.B.; Formal analysis, I.C.B. and D.V.; Investigation, F.S., V.B., A.N.R., and L.L.; Resources, M.T.O., V.G.; Data curation, M.B.; Writing—original draft preparation, I.C.B.; Writing—review and editing, V.G., B.A.S.; Visualization, D.V.; Supervision, D.M.; Project administration, M.T.O., V.G.; Funding acquisition, D.M., V.G. All authors have read and agreed to the published version of the manuscript.

Funding: This work was supported by research grants of the Romanian National Authority for Scientific Research and Innovation, CNCS/CCCDI—UEFISCDI, project numbers: 20PCCDI/2018 and PN-III-P2-2.1-PED-2019-0022, within PNCDI III and COFUND-M-ERA.NET II-HEAMODELL (1).

Conflicts of Interest: The authors declare no conflict of interest. The funders had no role in the design of the study; in the collection, analyses, or interpretation of data; in the writing of the manuscript, or in the decision to publish the results.

References

1. Miracle, D.B.; Senkov, O.N. A critical review of high entropy alloys and related concepts. *Acta Mater.* **2017**, *122*, 448–511. [[CrossRef](#)]
2. Gorse, S.; Couzinié, J.P.; Miracle, D.B. From high-entropy alloys to complex concentrated alloys. *Comptes Rendus Phys.* **2018**, *19*, 721–736. [[CrossRef](#)]
3. Gorse, S.; Miracle, D.B.; Senkov, O.N. Mapping the world of complex concentrated alloys. *Acta Mater.* **2017**, *135*, 177–187. [[CrossRef](#)]
4. Senkov, O.N.; Senkova, S.V.; Woodward, C.; Miracle, D.B. Low-density, refractory multi-principal element alloys of the Cr-Nb-Ti-V-Zr system: Microstructure and phase analysis. *Acta Mater.* **2013**, *61*, 1545–1557. [[CrossRef](#)]
5. Senkov, O.N.; Senkova, S.V.; Miracle, D.B.; Woodward, C. Mechanical properties of low-density, refractory multi-principal element alloys of the Cr-Nb-Ti-V-Zr system. *Mater. Sci. Eng. A* **2013**, *565*, 51–62. [[CrossRef](#)]
6. Senkov, O.N.; Senkova, S.V.; Woodward, C. Effect of aluminum on the microstructure and properties of two refractory high-entropy alloys. *Acta Mater.* **2014**, *68*, 214–228. [[CrossRef](#)]
7. Li, R.; Gao, J.C.; Fan, K. Study to Microstructure and Mechanical Properties of Mg Containing High Entropy Alloys. *MSF* **2010**, *650*, 265–271. [[CrossRef](#)]
8. Youssef, K.M.; Zaddach, A.J.; Niu, C.; Irving, D.L.; Koch, C.C. A novel low-density, high-hardness, high-entropy alloy with close-packed single-phase nanocrystalline structures. *Mater. Res. Lett.* **2014**, *3*, 95–99. [[CrossRef](#)]
9. Feng, R.; Gao, M.C.; Lee, C.; Mathes, M.; Zuo, T.; Chen, S.; Hawk, J.A.; Zhang, Y.; Liaw, P.K. Design of Lightweight High-Entropy Alloys. *Entropy* **2016**, *18*, 333. [[CrossRef](#)]
10. Kushnerov, O.; Bashev, V. Effect of Al and Si additions and cooling rates on phase composition and properties of CuFeMnNi alloy. *Bull. Dnîpr. Univ.* **2016**, *24*, 68–74.
11. Tseng, K.K.; Yang, Y.C.; Juan, C.C.; Chin, T.S.; Tsai, C.W.; Yeh, J.W. A lightweight high-entropy alloy Al 20 Be 20 Fe 10 Si 15 Ti 35. *Sci. China Tech. Sci.* **2018**, *61*, 184–188. [[CrossRef](#)]
12. Sanchez, J.M.; Vicario, I.; Albizuri, J.; Guraya, T.; Garcia, J.C. Phase prediction, microstructure and high hardness of novel lightweight high entropy alloys. *J. Mater. Res. Technol.* **2018**, *8*, 795–803. [[CrossRef](#)]
13. Moravcikova-Gouvea, L.; Moravcik, I.; Omasta, M.; Veselý, J.; Cizek, J.; Minárik, P.; Cupera, J.; Záděra, A.; Jan, V.; Dlouhy, I. High-strength $\text{Al}_{0.2}\text{Co}_{1.5}\text{CrFeNi}_{1.5}\text{Ti}$ high-entropy alloy produced by powder metallurgy and casting: A comparison of microstructures, mechanical and tribological properties. *Mater. Charact.* **2020**, *159*, 110046. [[CrossRef](#)]

14. Zhang, Y.; Zhou, Y.; Lin, J.; Chen, G.; Liaw, P. Solid-Solution Phase Formation Rules for Multi-component Alloys. *Adv. Eng. Mater.* **2008**, *10*, 534–538. [[CrossRef](#)]
15. Yang, X.; Zhang, Y. Prediction of high-entropy stabilized solid-solution in multi-component alloys. *Mater. Chem. Phys.* **2012**, *132*, 233–238. [[CrossRef](#)]
16. Guo, S.; Liu, C.T. Phase stability in high entropy alloys: Formation of solid-solution phase or amorphous phase. *Prog. Nat. Sci. Mater. Int.* **2011**, *21*, 433–446. [[CrossRef](#)]
17. Poletti, M.G.; Battezzati, L. Electronic and thermodynamic criteria for the occurrence of high entropy alloys in metallic systems. *Acta Mater.* **2014**, *75*, 297–306. [[CrossRef](#)]
18. Dong, Y.; Lu, Y.; Jiang, L.; Wang, T.; Li, T. Effects of electro-negativity on the stability of topologically close-packed phase in high entropy alloys. *Intermetallics* **2014**, *52*, 105–109. [[CrossRef](#)]
19. Guo, S.; Ng, C.; Lu, J.; Liu, C.T. Effect of valence electron concentration on stability of fcc or bcc phase in high entropy alloys. *J. Appl. Phys.* **2011**, *109*, 1–5. [[CrossRef](#)]
20. Guo, S.; Hu, Q.; Ng, C.; Liu, C.T. More than entropy in high-entropy alloys: Forming solid solutions or amorphous phase. *Intermetallics* **2013**, *41*, 96–103. [[CrossRef](#)]
21. Singh, A.K.; Kumar, N.; Dwivedi, A.; Subramaniam, A. A geometrical parameter for the formation of disordered solid solutions in multi-component alloys. *Intermetallics* **2014**, *53*, 112–119. [[CrossRef](#)]
22. Zhang, C.; Zhang, F.; Chen, S.; Cao, W. Computational thermodynamics aided high-entropy alloy design. *JOM* **2012**, *64*, 839–845. [[CrossRef](#)]
23. Manzoni, A.; Daoud, H.; Mondal, S.; Smaalen, S.v.; Völkl, R.; Glatzel, U.; Wanderka, N. Investigation of phases in Al₂₃Co₁₅Cr₂₃Cu₈Fe₁₅Ni₁₆ and Al₈Co₁₇Cr₁₇Cu₈Fe₁₇Ni₃₃ high entropy alloys and comparison with equilibrium phases predicted by Thermo-Calc. *J. Alloys Compd.* **2013**, *552*, 430–436. [[CrossRef](#)]
24. Senkov, O.N.; Miller, J.D.; Miracle, D.B.; Woodward, C. Accelerated exploration of multi-principal element alloys with solid solution phases. *Nat. Commun.* **2015**, *6*, 1–10. [[CrossRef](#)]
25. Sun, W.; Huang, X.; Luo, A.A. Phase formations in low density high entropy alloys. *Calphad Comput. Coupling Phase Diagr. Thermochem.* **2017**, *56*, 19–28. [[CrossRef](#)]
26. Chen, H.; Mao, H.; Chen, Q. Database development and Calphad calculations for high entropy alloys: Challenges, strategies, and tips. *Mater. Chem. Phys.* **2018**, *210*, 279–290. [[CrossRef](#)]
27. Takeuchi, A.; Inoue, A. Calculations of Mixing Enthalpy and Mismatch Entropy for Ternary Amorphous Alloys. *Mater. Trans. JIM* **2000**, *41*, 1372–1378. [[CrossRef](#)]
28. Senkov, O.N.; Miracle, D.B. Effect of the atomic size distribution on glass forming ability of amorphous metallic alloys. *Mater. Res. Bull.* **2001**, *36*, 2183–2198. [[CrossRef](#)]
29. Mann, J.B.; Meek, T.L.; Allen, L.C. Configuration Energies of the Main Group Elements. *J. Am. Chem. Soc.* **2000**, *122*, 2780–2783. [[CrossRef](#)]
30. Mann, J.B.; Meek, T.L.; Knight, E.T.; Capitani, J.F.; Allen, L.C. Configuration energies of the d-block elements. *J. Am. Chem. Soc.* **2000**, *122*, 5132–5137. [[CrossRef](#)]
31. Melting Point. Available online: https://www.webelements.com/periodicity/melting_point/ (accessed on 4 June 2019).
32. Takeuchi, A.; Inoue, A. Classification of metallic Glasses by Atomic Size Difference, Heat of Mixing and Period of Constituent Elements and Its Application to Characterization of the Main Alloying Element. *Mater. Trans.* **2005**, *46*, 2817–2829. [[CrossRef](#)]
33. Fries, S.G.; Hurtado, I.; Jantzen, T.; Spencer, P.J.; Kumar, K.H.; Aldinger, F.; Liang, P.; Lukas, H.L.; Seifert, H.J. Present achievements, problems and perspectives associated with a semi-empirical study of the Al-Cu-Mg-Si-Zn light alloy system. *J. Alloys Compd.* **1998**, *267*, 90–99. [[CrossRef](#)]
34. Laissardière, G.T.d.; Nguyen-Manh, D.; Mayou, D. Effective medium-range Mn-Mn pair interaction induces pseudogap in the density of states of Al(Si)-Mn approximants. *J. Non. Cryst. Solids* **2004**, *334*, 347–351. [[CrossRef](#)]

